UNIVERSITY OF LEEDS

This is a repository copy of *Correlations among the mineralogical and physical properties of halloysite nanotubes (HNTs)*.

White Rose Research Online URL for this paper:
http://eprints.whiterose.ac.uk/110344/

Version: Accepted Version

Article:
Hillier, S, Brydson, R, Delbos, E et al. (6 more authors) (2016) Correlations among the mineralogical and physical properties of halloysite nanotubes (HNTs). Clay Minerals, 51 (3). pp. 325-350. ISSN 0009-8558

https://doi.org/10.1180/claymin.2016.051.3.11

© 2016 The Mineralogical Society. This is an author produced version of a paper published in Clay Minerals. Uploaded in accordance with the publisher's self-archiving policy.

Reuse
Unless indicated otherwise, fulltext items are protected by copyright with all rights reserved. The copyright exception in section 29 of the Copyright, Designs and Patents Act 1988 allows the making of a single copy solely for the purpose of non-commercial research or private study within the limits of fair dealing. The publisher or other rights-holder may allow further reproduction and re-use of this version - refer to the White Rose Research Online record for this item. Where records identify the publisher as the copyright holder, users can verify any specific terms of use on the publisher's website.

Takedown
If you consider content in White Rose Research Online to be in breach of UK law, please notify us by emailing eprints@whiterose.ac.uk including the URL of the record and the reason for the withdrawal request.

White Rose university consortium
Universities of Leeds, Sheffield & York

eprints@whiterose.ac.uk
https://eprints.whiterose.ac.uk/

Correlations among the mineralogical and physical properties of halloysite nanotubes (HNTs).

STEPHEN HILLIER[1,2*], RIK BRYDSON[3], EVELYNE DELBOS[1], TONY FRASER[1], NIA GRAY[1], HELEN PENDLOWSKI[1], IAN PHILLIPS[1], JEAN ROBERTSON[1] AND IAN WILSON[4]

[1]The James Hutton Institute, Craigiebuckler, Aberdeen AB15 8QH, United Kingdom
[2]Department of Soil and Environment, Swedish University of Agricultural Sciences (SLU), SE-75007,Uppsala, Sweden
3 Institute for Materials Research, SCaPE, University of Leeds, Leeds LS2 9JT, United Kingdom
[4]Withielgoose Farmhouse, Withiel, Bodmin, Cornwall, PL30 5NW, United Kingdom

.

ABSTRACT: Twenty one samples of relatively pure tubular halloysites (HNTs) from localities in Australia, China, New Zealand, Scotland, Turkey, and the USA have been investigated by X-ray diffraction (XRD), infrared spectroscopy (IR) and electron microscopy. The halloysites occur as cylindrical tubular forms with circular or elliptical cross sections and curved layers and also as prismatic tubular forms with polygonal cross sections and flat faces. Measurements of particle size indicate a range from 40 to 12700 nm for tube lengths and from 20 to 600 nm for diameters. Size distributions are positively skewed with means lengths ranging from 170 to 950 nm and mean diameters from 50 to 160 nm. Cylindrical tubes are systematically smaller than prismatic ones. Features related to order/disorder in XRD patterns e.g. as measured by a 'cylindrical/prismatic' (CP) index and IR spectra as measured by an 'OH stretching band ratio' are related to the proportions of cylindrical versus prismatic tubes and correlated with other physical measurements such as specific surface area and cation exchange capacity. The relationships of size to geometric form, along with evidence for the existence of the prismatic form in the hydrated state and the same $2M_1$ stacking sequence irrespective of hydration state (i.e. 10 vs 7 Å) or form, suggests that prismatic halloysites are the result of continued growth of cylindrical forms.

*E-mail: stephen.hillier@hutton.ac.uk

KEYWORDS: halloysite, nanotubes, HNTs, cylindrical, prismatic, polygonal, length, diameter, surface area.

Although it is probably less abundant in nature than kaolinite, the mineral halloysite is of widespread occurrence in many soils (Dixon, 1989) and also forms important economic accumulations in deposits mainly of hydrothermal origin (Wilson & Keeling, 2016). Halloysite has fascinated investigators ever since it was first discovered that, in obvious contrast to the other kaolin subgroup minerals, namely kaolinite, dickite and nacrite which occur primarily in planar platy or blocky forms, many halloysites adopt an unusual tubular morphology. Spheroidal halloysite is also very well documented especially from soils, but here our focus will be entirely on the tubular form of halloysite, increasingly referred to as halloysite nanotubes or 'HNTs' due to a rapidly expanding range of applications in a wide variety of technologies. Aside from its unusual morphologies, halloysite is also distinct amongst the other kaolin polytypes in that it is hydrated with H_2O molecules positioned in the interlayer space between the fundamental 1:1 layer combination of tetrahedral and octahedral sheets that form the basic kaolin structure. Indeed, according to Churchman & Carr (1975) the single most important characteristic that identifies, defines, and distinguishes halloysite as a distinct kaolin mineral is the presence, or evidence of the former presence, of molecules of H_2O in the interlayer space. Interlayer H_2O in halloysite is exceedingly labile and in response to changing environmental conditions, both naturally in the field or subsequently in the laboratory, it is readily and irreversibly lost. In its fully hydrated state halloysite contains two interlayer H_2O molecules accounting for 12.25 wt. % of the molecular formula unit which can be written as $Al_2Si_2O_5(OH)_4 \cdot 2H_2O$. With this full complement of interlayer H_2O halloysite has a primary basal spacing, as observed in X-ray diffraction (XRD) patterns, of approximately 10Å. Because the loss of the interlayer H_2O is generally not a

reversible process, depending on the handling and storage history halloysites are most commonly observed with lower H_2O contents by mass and smaller basal spacings. In an essentially dehydrated state the layer spacing approaches the 7Å basal spacing characteristic of all other kaolin polytypes. Due to this variability of basal spacing as a function of the degree of hydration it has been recommended that the approximate basal spacing should be appended to the name, for example halloysite (10Å), and halloysite (7Å) would signify hydrated and dehydrated specimens respectively (Bailey, 1980). In the older literature some workers referred to fully hydrated halloysite as 'endellite' and the dehydrated form as 'metahalloysite', but both of these terms are now regarded obsolete (see Brindley (1984) page 153 for a brief summary of halloysite nomenclature past and present). Most investigators now accept that the primary form of halloysite, i.e. at the time of its formation, is the fully hydrated 10Å form and that other forms with less H_2O and consequent smaller basal spacings have undergone some degree of post formation dehydration.

Although there are earlier reports, Bates *et al*., (1950) are usually attributed with discovering the tubular morphology of halloysite perhaps because they immediately offered an explanation for the cylindrical form as being the result of a mechanism to compensate for the lateral misfit between a larger tetrahedral and a smaller octahedral sheet of the basic kaolin 1:1 layer type. More recently Singh (1996) has suggested that rolling is energetically favored in halloysite since it offers the least resistance from Si-Si Coulombic repulsion. Putting aside the various explanations for the curvature of the layers and the consequent rolled or cylindrical form of halloysite it was nonetheless evident, even in the earliest literature on halloysite, that in addition to cylindrical tubes,

polygonal tubes with a prismatic structure exhibiting flat faces present another distinctive morphology of tubular halloysite (Bates & Comer, 1957; Hoffman *et al*., 1962; Chukhrov & Zvyagin 1966; Bailey 1990; Kogure *et al*., 2013).

In the present manuscript it is demonstrated that there are systematic relationships between the XRD patterns, infrared (IR) spectra, cation exchange capacity (CEC), particle size, surface area and porosity of tubular halloysites all of which are fundamentally related to the proportions and structures of cylindrical tubular versus prismatic polygonal tubular forms present in any given sample. Furthermore, it is emphasized that prismatic forms are not rare morphologies, but occur widely in many halloysite samples. The understanding presented of the interrelation of form (cylindrical versus prismatic) and properties should be useful in the wide variety of emerging applications of HNTs and the relationships demonstrated may also help to constrain models of tubular halloysite formation and growth.

MATERIALS AND METHODS

Twenty one different samples of tubular halloysite were studied. The samples were obtained from halloysite occurrences in Australia, China, New Zealand, Scotland, Turkey and the USA including various commercially exploited deposits, (Table 1).

Sample 1Au is from the Eucla basin in S. Australia and is equivalent to sample CLA-1 described previously by Keeling et al., (2011), and Pasbakhsh et al., (2013). Six samples originate from halloysite deposits in China, including the Zunyi region (2Ch), Dafang region (3Ch, 4Ch) the Bifa deposit (5Ch) the Wan Jiar deposit (6Ch) (Wilson, 2004; Wilson & Keeling 2016, this volume) and one sample (7Ch) is from an unknown

location in China. The former were collected by one of the current authors (Ian Wilson), and the latter was supplied by IMERYS, courtesy Jeremy Hooper. Three samples are from New Zealand. The sample supplied by IMERYS (8NZ) is believed to originate from the well-known Matauri Bay deposit, North Island, as are the other two samples. That supplied by Jock Churchman (9NZ) is also described in Joussein *et al*., (2005) where it corresponds to the sample shown in Figure 5a (incorrectly captioned as 5c in Joussein *et al.*, 2005, Churchman pers. comm. 2008), whilst the exact source of the third sample (10NZ) is unknown. The sample from Scotland (11Sc) is from the Macaulay Collection at the James Hutton Institute, it originates from Hospital Quarry, Elgin, as previously described by Hillier & Ryan (2002) and was collected by Heddle (Heddle, 1882); a counterpart 'Spec. 493.1' of this sample is held in the National Museum of Scotland in Edinburgh. A recent visit to the site showed that this halloysite occurs in a brecciated zone of Permian sandstone. Two samples were obtained from deposits in Turkey, one (12Tu) of unknown provenance provided by IMERYS whilst the other (13Tu) originates from the Balikesir region, halloysite deposits of which have been previously described by Ece & Schroeder (2007). The remaining eight samples are all from the USA. Seven of them originate from the Dragon Mine in Utah, five of which were supplied by Applied Minerals, who now own and operate the mine. Additional samples from the Dragon mine include one (19US) supplied by IMERYS, and one which can be purchased from Sigma Aldrich (20US). The remaining sample (21US) from the USA is from the Bovill deposit Idaho, USA, supplied courtesy of IMinerals Inc. Chemical analyses made by X-ray Fluorescence (XRF), all using fused glass beads but made in a variety of different laboratories, were available for all samples. Due to differences in reporting, such as

including or not including loss on drying or loss on ignition, for ease of comparison the analyses are compiled in Table 2 normalized to a theoretical kaolinite composition.

X-ray diffraction

For powder XRD analyses 3g samples were McCrone milled for 12 minutes in ethanol and the resulting slurry spray dried at 60°C directly from the mill to form random powder specimens (Hillier, 1999). Note that drying at 60°C from ethanol results in all halloysites dehydrating to the 7Å form. Specimens were loaded into a Siemens D5000 and scanned between 2 and 70°2θ, counting for 2 seconds per 0.02° step using Co Kα radiation selected by a diffracted beam monochromator. Diffraction patterns were also recorded from 3-70°2θ in 0.0167° steps on a Panalytical Xpert Pro diffractometer using Ni filtered Cu radiation and counting for 100 seconds/step using an Xcelerator detector. Peak positions, intensities and peak width as Full Width at Half Maximum (FWHM) were measured using Bruker Diffrac Eva software, using data obtained from the D5000. Quantitative mineralogical analysis of all samples was made by a full pattern fitting method using experimental patterns as standards for all minerals identified. The method is as described in Omotoso *et al*., (2006) by participant 18, 2nd place finisher in the 3rd Reynolds Cup round robin, but without the addition of an internal standard. For halloysite standard patterns were extracted from the sample set, based on the best examples and on verification of purity by multiple analytical methods. Patterns for all other minerals were obtained from examples held in the Macaulay mineral collection. In all cases extensive cross checks on purity were performed. The presence of absence of kaolinite in the samples was also verified by formamide intercalation (Churchman *et al*., 1984). Samples

were gently ground under a small amount of water to produce a slurry that was pipetted onto a glass slide, once air dry the specimens were scanned from 5-15°2θ on the Panalytical Xpert Pro diffractometer detailed above with a total scan time of 9 minutes. The sample was then sprayed with a formamide/water (10%) solution, allowed to stand for 40 minutes and then rerun on the diffractometer using the same 9 minute scan, as such total exposure time to formamide was approximately 50 minutes.

Transmission Electron Microscopy

Samples for transmission electron microscopy (TEM) were prepared by dispersing powders in methanol and drop casting onto holey carbon supports on copper TEM grids. This preparation method was compared with a procedure involving simply dusting powders onto TEM grids; for both methods similar results were obtained. TEM specimens were examined using bright field, dark field and phase contrast imaging, selected area electron diffraction (SAED) and energy dispersive X-ray (EDX) spectroscopy at 200 kV using a FEI CM200 field emission TEM/STEM. Electron diffraction patterns were recorded on photographic film.

Scanning Electron Microscopy

For SEM secondary electron imaging either powders or fractured surfaces of specimens were mounted onto standard aluminum stubs using double-sided carbon tab as the adhesive and sputter coated with a thin layer of platinum to reduce charging under the electron beam. Analysis was conducted using a Carl Zeiss Sigma VP Field Emission

Scanning Electron Microscope (FEG-SEM) in variable pressure mode at an accelerating voltage of 15kV.

For image analysis of particle size distributions specimens of a few milligrams were prepared by 5 minutes ultrasonic dispersion into 100ml of deionized water to which two drops of 'Calgon' were added, resulting in dispersions with turbidity readings varying between 7 and 96 nephelometric turbidity units (ntu). A single drop of the dispersion was then placed on a nickel TEM grid (90 μm diameter square holes) supported on a silicon wafer and the drop allowed to air dry in a desiccator. The grid serves to break the drying droplet into smaller micro droplets and seems to assist in obtaining more homogenous dispersion of particles on the surface of the silicon wafer to facilitate subsequent image analysis. The wafers were coated with an Au/Pd mixture and examined by SEM. Image analysis was performed using the freely available ImageJ software (Rasband 1997-2015). All images were converted to 8 bit binary, calibrated using the scale bars, adjusted manually for threshold, filtered manually to reduce noise, and converted to binary images. Distributions of particle length and diameter were measured on multiple images for each sample using the particle analysis function of ImageJ by fitting ellipsoids. Additionally, maximum and minimum length and maximum and minimum diameters of halloysite particles were measured by a manual survey of each set of images. These values were then used as limits to filter the semi-automated particle measurements obtained using ImageJ such that apparently larger or smaller particles than the manually determined limits were rejected. Particles with aspect ratios less than 1.5 were also rejected to assist in the elimination of aberrant measurements, such as from particles of the wrong shape, or of groups of overlapping particles.

Surface Area and Porosity

Surface area and porosity were measured by nitrogen gas adsorption using a Coulter SA 3100 Plus instrument. Surface area was calculated according to the BET equation using five points in the relative pressure range 0.05 to 0.20, and pore size distributions were calculated from the adsorption isotherms according to the BJH model. Prior to analysis all samples were outgassed under vacuum at 100°C for 1 hour.

Infrared Spectroscopy

A small quantity of each sample in as received state was transferred, in turn, on to the sample area of a single reflection diamond attenuated total reflectance (DATR) accessory, fitted with a KRS-5 substrate. IR spectra were then recorded using a Bruker Vertex 70 Fourier Transform Infrared (FTIR) Spectrometer in the mid infrared region (4000 to 400 cm^{-1}). The FTIR spectrometer is dry air purged to prevent interference in the IR spectra caused by water vapour and CO_2. An ATR correction, to allow for the variation in depth of penetration with wavelength, was applied to all IR spectra using OPUS software (Bruker).

Cation Exchange Capacity

CEC was measured using a cobalt hexammine trichloride method based on the ISO 23470 standard at ambient sample pH, wherein the exchangeable cations on the sample are replaced by trivalent cobalt hexammine ions and the CEC of the sample is determined by

absorption colorimetry. The sample reference state is oven dried at 105°C. The method is described in more detail in Gray *et al*., (2016, this volume)

RESULTS

Morphology by SEM

Comparison of the samples in the SEM reveals that some samples are composed of relatively fine tubular forms and are circular or oval in cross section, whilst others are very obviously prismatic in form with long flat faces giving rise to angular polygonal cross sections and ends (Figure 1). Other samples appear to be mixtures of types showing the presence of both cylindrical and polygonal forms. It is also apparent, especially when occurring together, that cylindrical forms are typically narrower in diameter than polygonal prismatic ones. Cross sections of around 40-70 nm diameter seem typical for cylindrical tubes, whereas diameters of up to 250 nm are not uncommon in samples dominated by the polygonal prismatic habits. In an effort to gain more quantitative data on the size distributions of the tubes, in and between samples, image analysis was conducted on dispersed specimens from each sample.

SEM image analysis

Images of the dispersed specimens confirm that all the samples are composed of predominantly tubular forms. Manual measurements of maximum and minimum lengths and diameters indicated an overall range from 40 to 12700 nm (0.04 to 12.7 μm) for tube lengths and from 20 to 600 nm (0.02 to 0.60 μm) for tube diameters. Examples of dispersed specimens are shown in Figure 2 and corresponding histograms for lengths and

diameters in Figures 3 and 4. Summary measurements and descriptive statistics for particle size distributions in all samples are given in Table 3.

Although there is wide variation in each sample data set, in general in any given sample longer tubes tend to be thicker than shorter tubes. Additionally, all size distributions for both length and diameter are highly positively skewed (Figure 3, 4, Table 3). Log transformation of the data results in more symmetrical distributions, but only two samples (2Ch, 15US) of the log transformed data passed normality tests (Shapiro-Wilk) which indicate that the primary distributions are log normal ones. Nonetheless, given that all the primary size distributions are highly skewed all samples are summarized by back transformed means and standard deviations of the log transformed data (Table 3); in contrast to the plus or minus standard deviation of a normal distribution, the standard deviations are more usefully understood as dividing or multiplying the mean to describe the skewed dispersion about it (Limpert *et al*., 2001). Also reported for comparison are median values of the primary untransformed data, which in all cases are very similar to the log back-transformed means. In summary mean lengths range from 170 to 950 nm (0.17 to 0.95 μm) and mean diameters from 50 to 160 nm (0.05 to 0.16 μm). Notably five of the six samples from China have mean lengths and diameters less than or equal to 260 and 50 nm (0.26 and 0.05 microns) respectively, indicating that the Chinese halloysites tend to be composed of relatively small tubes. Additionally, mean lengths and mean diameters for the sample set as a whole are correlated. Mean aspect ratios range from 2.6 to 7.4. Also tabulated are average aspect ratios of the top 10% of measurements from each sample ranging in this case from 5.7 to 17.2. In all samples these maximum aspect ratios are close to 2.4 times the mean values.

Also given in Table 3 are specific surface areas calculated from the particle size distributions. The calculations assume cylinders with a lumen diameter of 17.5 nm which is the average of the theoretical lumen diameter calculated by Bailey (1990) based on the dimensions of tetrahedral and octahedral sheets and the ideal radius of curvature to accommodate their misfit for rolling around either the a or the b axis.

At high magnifications the images of the dispersed samples also reveal various features of the morphology of individual particles and their inter-relationships (Figure 5). These include the obvious prismatic forms of the larger particles and the occurrence of thinner tubes protruding from the central cores of thicker ones, often forming spindle like structures, previously noted for example by Dixon & McKee (1974). In most cases the smaller thinner tubes appear cylindrical. In other cases small cylindrical tubes intersect at an angle with larger prismatic ones, and occasionally curved moulds of these intersections are also visible in some prismatic particles where intersecting tubes have presumably become detached during sample preparation. A final feature is the angular terminations of the larger tube edges and the outlines of pseudo hexagonal forms on the surfaces of some tubes similar to features observed for example by Unal-Ercan et al., (2016). Further details of several of these features are revealed in TEM images (see below).

Mineralogical composition by XRD

XRD analyses by full pattern fitting are consistent with the microscopy data indicating that all of the samples are composed predominantly of halloysite (Table 4). Five of the samples (2Ch, 3Ch, 6Ch, 14US and 15US) appear to be essentially pure halloysite

according to XRD whilst nine others (1Au, 4Ch, 5Ch, 7Ch, 8NZ, 11Sc, 13Tu, 17US and 19US) are 98% plus pure halloysite. Impurities in the remaining samples consist of kaolinite, gibbsite, alunite, quartz, and cristobalite, and possibly traces of woodhouseite or a similar phosphate, the amounts being too small for certain identification by XRD alone. Most of the samples only contain trace amounts of quartz, but two of the samples from New Zealand (9NZ, 10NZ) are consistent in containing more than 5% quartz along with similar amounts of cristobalite, whilst one of the samples from Turkey (12Tu) also has 4% quartz. Perhaps not unexpectedly, kaolinite is the most common impurity and its presence was confirmed in the same samples by the formamide test. One of the samples from the US Dragon Mine (US18) was deliberately included in the set because it appears to contain about 20% kaolinite based on full pattern fitting, a value that appears corroborated by the formamide test, but seem somewhat at odds with the electron microscopy observations which suggest a lower kaolinite content.

XRD characteristics

Since the samples are all relatively pure halloysite it is instructive to compare and contrast various features of their random powder XRD patterns which can be related directly to the characteristics of the halloysite present. In the 'as received' state the samples exhibited various states of hydration/dehydration, some showing large proportions of 10Å halloysite others showing only peaks for the 7Å form. Halloysites are well known to dehydrate rapidly (see Figure 1 of Wilson & Keeling (2016), this volume) so because of the dependence of basal peak position on the rather variable, often unknown, collection and storage history of different samples it made little sense to

compare diffraction data across the set in the ‘as received state’. However, examples of diffraction patterns of one predominantly cylindrical form (5Ch) and one predominantly prismatic form (17US), as determined by SEM examination, are shown both hydrated (as received) and dehydrated (oven dried 105°C) in Figure 6.

Across the entire set of samples measurements were made on the random powder specimens that were prepared by spray drying at 60°C since after this process all samples are consistently in the 7Å form. Nonetheless the observed basal spacings of the spray dried samples are quite variable ranging between 7.193 and 7.667 Å (Table 4). Measurements conducted on two standard kaolinites (KGa-2, and KGa1b) gave values of 7.184 and 7.169 Å, i.e. slightly smaller than any spacing recorded for halloysite. Peak widths (Full Width at Half Maximum (FWHM)) are also rather variable ranging from 0.501 to 1.498 Å, compared to 0.326 and 0.254 Å for the reference kaolinites (Table 4). Additionally, peak positions and peak widths are correlated. Comparison of the XRD patterns of hydrated and dehydrated forms (Figure 6) confirms the summary of Brindley (1984) that the patterns of the variously hydrated forms differ mainly in the positions of the basal reflections and rather little in the broadly spreading non-basal diffraction bands, though some effects on the latter are apparent. However, a comparison of either 10 or 7 Å patterns for the two different tube morphologies indicates that there are modulations of non-basal diffraction bands, particularly evident in the 20, 13 band, for the prismatic types compared to the cylindrical ones. Thus the 20,13 diffraction band between about 2.6-2.3 Å varies between a broad rounded maxima (cylindrical form) with a leading edge, reminiscent of the turbostratic two dimensional diffraction bands observed for smectites, to a more modulated band with at least two distinct peak maxima in addition to the

peaked leading edge of the band (prismatic form). Importantly, these differences are apparent irrespective of the state of hydration (Figure 6), although we have not observed prismatic samples with modulated bands that were in a completely hydrated (10Å) form.

The extent to which the modulation of the band is developed may be quantified by a simple index termed 'CP' (cylindrical-prismatic) the measurement of which is illustrated in the insert to Figure 6 with values for all samples tabulated in Table 4. The index is defined as background subtracted minimum/(minimum + maximum) intensities where, due to the variable characteristics of the 20,13 band, the minimum and maximum intensities are deliberately and necessarily measured from the lowest 'valley' and highest peaks of the entire 20,13 band, rather than at fixed positions. In the spray dried random powder preparations a small number of samples also show discernable but generally weak 021 and $\bar{1}12$ reflections at d-spacings of approximately 4.26 and 4.09 Å in the tail of the 02,11 band situated between about 4.5 and 3.8Å. These include the sample 1Au from Australia, sample 3Ch from the Dafang region China, sample 11Sc from Scotland, and samples 17US and 18US from the Dragon mine, Utah USA (Figure 7). Sample 17US from the Dragon mine also shows a relatively strong peak at approximately 4.35Å in the 'as received' sample which was largely hydrated, this peak being indexed as the equivalent 021 peak (Bailey, 1990) of the 10Å hydrated form (Figure 7). One additional feature of the XRD patterns also worthy of mention is the variability in position and breadth of the 06,33 band. For the two reference kaolinites the center of gravity of this band was measured at about 1.489 to 1.488 Å. In comparison the values for the halloysites extend to smaller d-spacings of around 1.483 Å with the smallest spacings always also associated with the broadest peaks.

TEM observations

TEM was only conducted on a selected number of samples (3Ch, 11Sc, 14US, 18US). It confirmed the apparent two layer structure ($2M_1$) revealed in electron diffraction patterns (Figure 8) as shown previously by other workers, and also revealed further details of the textures observed by SEM. In particular the electron transparent central lumen is clearly visible in tubes from both cylindrical and prismatic examples, and some of the larger prismatic varieties show obvious hexagonal plate like features arranged in apparent crystallographic alignment with the tube axis, particularly at tube endings where the edges of plate like terminations appear oriented at right angles to the tube axis. Similar features were documented by Dixon & McKee (1974) who interpreted them as a continuation of 'hexagonal growth edges'.

FTIR characteristics

The IR spectra of the various halloysites studied also vary in their characteristics (Figure 9) and examination of the OH stretching region, in particular (3800-3400cm^{-1}) shows that certain features make some spectra clearly distinct from others. Thus several halloysite spectra differ very clearly from IR spectra of kaolinite by showing just two prominent OH stretching bands, arising from structural OH groups, near 3620cm^{-1} and 3690cm^{-1} with the lower frequency 3620cm^{-1} band obviously more intense than the higher frequency 3690cm^{-1} band. In contrast, other spectra show one or two additional weak intermediate OH stretching bands near 3670 and 3653 cm^{-1}, which also occur in kaolinite spectra due to out of phase stretching which is split due to imperfect 3 fold symmetry

(Farmer, 1974). When only one intermediate band is apparent it is the higher frequency 3670 cm^{-1} band. In such spectra with intermediate bands the OH stretching band near 3690 cm^{-1}, arising from the surface hydroxyls (Farmer, 1974) tends to show increased intensity relative to the inner OH stretching band near 3620 cm^{-1} which arises from the inner hydroxyl, and both bands also have a tendency to sharpen. There are also indications that the vibrations giving rise to the 3620 and 3690 cm^{-1} bands absorb at slightly lower frequencies in spectra of this type compared to those where intermediate OH stretching bands are not present. The observed change in relative intensity of the two main OH stretching bands, together with the appearance of the weak intermediate bands, are features that suggest that the corresponding samples possess significant 'well-ordered' kaolinite-like character. Indeed, the weak OH deformation band near 935 cm^{-1} in these spectra (assigned to a bending vibration of surface OH groups) that is also present in kaolinite spectra, is not detectable in the halloysite spectra with no intermediate OH stretching bands presumably due to uncoupling of the surface OH bonds (Farmer, 1974). Therefore this feature also presents evidence for the presence of kaolinite-like character in those halloysite IR spectra in which it appears.

In addition to bands relating to structural OH groups, the OH stretching region also shows OH stretching bands arising from H_2O molecules. The medium intensity absorption band near 3550 cm^{-1} is assigned to the OH stretching of halloysitic interlayer 'hole water' (Costanzo et al., 1984; Giese, 1988) that probably forms weak hydrogen bonds with the oxygen atoms of the siloxane tetrahedral sheet and possibly with the surface hydroxyls of the octahedral sheet in the next 1:1 layer. The corresponding OH bending band is taken to be the weak sharp band near 1650 cm^{-1}. As far as kaolins more

generally are concerned, it is worth noting that these distinctive bands due to 'hole water' are the only bands that are entirely unique to halloysite. The weak and broad absorption near 3430 cm-1 is tentatively assigned to the OH stretching of 'associated' interlayer H_2O (Costanzo et al., 1984), with the low frequency indicating the presence of relatively strong hydrogen bonding; the corresponding OH bending band is near 1630 cm^{-1}. The structural 'hole water' OH stretching band also appears to be sharper in spectra with kaolinite-like character suggesting a more ordered structure overall.

The presence/absence of the intermediate OH stretching bands as well as the 935 cm^{-1} OH bending band along with an 'OH stretching band intensity ratio', measured as shown in the insert to Figure 9 (but in absorbance rather than transmission), provides an empirical means of differentiating the two halloysite types (Table 4). To some extent, the proposed 'OH stretching band intensity ratio' may be affected by the degree of hydration, and also by possible orientation effects but the relative reproducibility of the IR sample handling procedure would certainly reduce any effect of sample orientation. It should also be noted that minor/trace amounts of gibbsite or kaolinite would serve to either reduce or increase the ratio respectively. Despite the possible influence of these effects the 'OH stretching band intensity ratio' is nonetheless a simple way to portray the classification of the different samples according to IR spectroscopy.

Surface area and porosity by N_2 adsorption

Specific surface area and porosity measurements for the sample set are given in Table 5. BET surface area ranged from approximately 15 to 90 m^2g^{-1} and BJH specific pore volume from approximately 0.06 to 0.30 ml^3g^{-1}. Also included in Table 5 are measured

values for the most frequent pore diameter (adsorption isotherm). This value was readily determined for the majority of samples which all show a peaked distribution within the accepted size range of the HNT lumen diameter (5-30nm in the differential pore volume plots), however, six samples showed more gradually sloping, flatter distributions, with no obviously discernable maximum and are labelled 'not measurable' in Table 5. Some examples of the differential pore volume plots are shown in Figure 10. The range of most frequent pore diameter was 8.9 to 16.5 nm and the average 13.5 nm. Hydraulic pore diameters (assuming cylindrical pores ($4Vp/A_{BET}$) range from 7.0 to 26.6 nm with an average of 15.1 nm. The specific pore volume for pores within the size range from 5-30 nm in diameter is also tabulated as well as the % lumen space calculated for each sample as per Pasbakhsh *et al*., (2013), i.e. assuming a density for halloysite of 2.6 gcm^{-3} which corresponds to a structure completely dehydrated of any interlayer water. A final feature of note is that some samples showed obvious hysteresis between the adsorption and desorption isotherms, whilst others showed branches that were more or less coincident between adsorption and desorption. Examples of the different types are shown in Figure 11, and the relative extent of hysteresis, quantified by calculating the difference between the areas under the two curve branches at relative pressures greater than 0.4, is given in Table 5.

CEC

Measured CEC values for 20 of the halloysites are also listed in Table 5, they vary between 2.0 and 9.3 cmol (+) kg^{-1}. Table 5 also includes CEC values normalized to a specific surface area of 50 m^2g^{-1} which approximates the average BET surface area of the

sample set, and this narrows the range of values to between 3.6 and 7.4. By a similar calculation the CEC of sample 11Sc, which was not available in sufficient mass for CEC measurement is predicted, based on its low surface area, to be about 1.6 cmol (+) kg^{-1}.

DISCUSSION

Halloysite has long been described in a wide variety of different habits but its early recognized tubular form (Bates et al., 1950) is undoubtedly its most common form (Joussein et al., 2005). Additionally, its current nomenclature in many technological applications as halloysite nanotubes or 'HNTs' fundamentally acknowledges the importance placed on its nano tubular shape (Churchman 2015). Shortly after the tubular form of halloysite was recognized it was also recognized that the character of the tubes varied between different samples. Some tubes were cylindrical, i.e. with circular or elliptic cross sections, others had angular polygonal or polyhedral cross sections, reflecting elongated prismatic forms (Bates & Comer, 1957, Hoffman *et al*., 1962; Chukhrov & Zvyagin, 1966; Bates, 1971; Dixon & McKee, 1974) the faces of which are all of index (001) (Chukhrov & Zvyagin, 1966). Furthermore, it was noted that the prismatic forms (often termed laths by some authors of this era) tended to correspond to specimens of 'metahalloysite', a now defunct term used historically for the dehydrated 7Å form of halloysite. It was also often remarked that specimens of 'metahalloysite' typically showed more order in their XRD patterns compared to examples of the fully hydrated 'endellite', now termed halloysite (10Å) and from which, either in nature or in the laboratory, 'metahalloysite' was believed to be derived by dehydration. Collectively, these observations led many early workers to suggest that the prismatic faces were

developed by flattening during dehydration and that this process was implicitly linked to the increased order observed for 'metahalloysite'. Such increased order was mainly reflected in sharper basal reflections and greater resolution of non-basal reflections. Additionally, peaks that are characteristic of the two layer ($2M_1$) structure of halloysite (Bailey, 1990; 1993), or at least some tendency towards this mode of stacking (Kogure et al., 2013) as commonly recorded in electron diffraction patterns of all types of halloysite (Chukhrov & Zvyagin, 1966; Kohyama et al., 1978), were occasionally observed by XRD for prismatic specimens in the tail of the 02,11 diffraction band, a feature first noted by Honjo et al., (1954). The idea that dehydration was responsible for the prismatic tubular form of halloysite was reiterated by Bailey (1990), although he added that 'at least some of the faces appear too regular and flat for such an origin'. Indeed the possible link between dehydration and cylindrical versus prismatic form is still being considered, with Kogure et al., (2013) in a detailed study of a prismatic halloysite from Russia suggesting that the tendency towards two layer periodicity in the layer stacking sequence may have its origins in the conversion of originally cylindrical forms to prismatic ones by a 'long term ripening process' with dehydration as a key step.

The samples examined in the present investigation include both cylindrical and prismatic tubular types (Figures 1, 2, 5, 8). With respect to the XRD patterns of kaolinites they all show the usual, though subtle, indicator characteristics of halloysite including slightly larger d-spacings and considerably broader basal peaks (Table 4). Both of these features may be related mainly to residual interlayer H_2O molecules and, in the case of the samples composed primarily of cylindrical tubular forms, curvature of the layers as an another type of disorder is also likely to contribute to these diffraction

characteristics. Additionally, the prismatic polygonal forms are characterized by 20,13 bands that are modulated into peaks, although the degree of modulation, or peak definition, as measured by the proposed 'CP' index is not as pronounced as it is in samples of pure kaolinite (Table 4), including poorly ordered kaolinite, such that the index also appears to provide a ready distinction of pure kaolinite from samples containing halloysite. Cylindrical halloysites in contrast show 20,13 bands that are composed of a single broad scattering region following the peaked leading edge of the 20,13 band. This latter type of pattern is certainly the type described by Brindley & Robertson (1948) for 'metahalloysite' as one consisting only of basal (00l) reflections and (hk) bands. In terms of explaining the different types of diffraction patterns, the modulation of the 20,13 band into peaks in the prismatic examples is believed to simply reflect the presence of flat faces and the construction of prismatic tubes from radial sectors, as shown by other investigators via examination in the TEM (Chukhrov & Zvyagin 1966; Kogure *et al*., (2013). Thus the diffraction band for prismatic forms contains some peaks that are of the type (hkl) (Brindley & Robinson 1948). In contrast for the cylindrical tubes it is assumed that the XRD pattern is also affected by disorder due to the curvature of the layers and as such there are no reflections with index (hkl). Thus the proposed 'CP' index clearly distinguishes between predominantly cylindrical versus predominantly prismatic halloysites as well as distinguishing both types from kaolinite. Distortions of the halloysite diffraction patterns due to layer curvature may also explain the broader shape and slightly smaller d-spacings recorded for the 06, 33 bands of predominantly cylindrical compared to predominantly prismatic forms. With respect to the 06, 33 peak position we speculate that rolling with the b axis aligned along

the tube axis, as is commonly observed, might also result in some contraction of the structure in this direction. The presence of planar faces in prismatic samples will also explain why some halloysites appear to show more preferred orientation in X-ray powder patterns relative to others in terms of basal/non-basal intensity ratios when prepared by methods that do not guarantee random powder specimens, a point remarked upon previously by Dixon & McKee (1974). From the above discussion it should be clear that Brindley & Robinson (1948) equated the XRD pattern of all 'metahalloysites' with the type of XRD pattern corresponding to dehydrated cylindrical forms and, despite noting 'additional peaks' in some 'metahalloysite' samples, they preferred to reserve judgement on their significance. These extra peaks most probably indicate that these other 'metahalloysite' samples contained tubes of predominant prismatic morphology. Indeed, a reluctance to associate any order with the diffraction patterns of halloysite persisted for some time with de Souza Santos et al., (1965) preferring the description 'tubular kaolinite' for a sample from Brazil, that appears in hindsight to be an excellent example of a prismatic halloysite. In a related publication Brindley *et al*., (1963) had earlier identified type 'C' and type 'D' XRD patterns equating them with 'rolled' and 'tubular' halloysite, but the study was more focused on the potential for 'order' to be more apparent than real due to halloysite frequently being admixed together with kaolinite. Again with hindsight, Brindley's type 'C' patterns relate to prismatic and type 'D' to cylindrical forms of halloysite, respectively. With modern methods of full pattern fitting of XRD data the various differences present in the diffraction patterns of halloysites relative to those of kaolinite are sufficiently distinct to allow successful quantification of mixtures of kaolinite and halloysite.

Measurements of length and diameter by image analysis show that there is a wide variation in tube sizes amongst the samples. However, the range of values obtained are very comparable to the values for thirteen samples measured by TEM (400 measurements per sample) by Bates & Comer (1957). Calculation of specific surface areas from the particle size distribution data gave values that were reasonably similar to those measured by N_2 adsorption and this provides something of a further validation of the particle size data obtained from the image analysis method. Bates & Comer (1957) also found a high correlation between mean tube length and mean tube diameter and commented that this was indicative of a 'structural relationship between the two parameters'. For comparison the data of Bates & Comer (1957) for mean particle length and diameter are shown alongside data from the present study in Figure 12. Neither Bates & Comer (1957), nor Bates (1971) who drew additional attention to this relationship, offered any further explanation. Presumably, the structural relationship envisaged is simply one reflecting processes of crystal growth i.e. halloysite tubes that have grown longer have also tended to grow thicker. However, we are reminded that exceptions will and do undoubtedly exist e.g. the exceptionally long (30 μm length) and thin (0.03 μm diameter) Patch halloysite described in detail by Norrish (1995).

In recognition that some samples are mixtures of different morphological forms the proposed 'CP' index provides a simple way to rank the samples and compare the XRD characteristics to other measurements, such as size, surface area, and CEC. In terms of the particle size data these comparisons show that the 'CP' index is correlated with both mean and maximum diameters and lengths of halloysite particles. The correlation demonstrates that cylindrical halloysites are typically smaller than prismatic

ones confirming the impression gained from cursory examination of the different forms under the SEM (Figure 1). It is pertinent to note that Dixon & McKee (1974) in a detailed TEM study of a tubular halloysite from Wagon Wheel Gap, Colorado, also commented that smaller tubes were more nearly circular in cross-section that thicker ones. Perhaps not unexpectedly, given the correlations with particle size, specific surface area and CEC are also well correlated with the 'CP' index measured from XRD data. Thus cylindrical halloysites tend to have larger surface areas and larger CEC's compared to prismatic examples. A correlation matrix for the main diffraction, size, adsorption and IR spectroscopic data of the present study is given in Table 6. Documentation of these systematic relationships between tube form and size suggest that prismatic tubular forms may be interpreted as tubular forms that have simply grown larger than cylindrical forms, a point we shall return to later. Furthermore, it is evident that prismatic forms are just as common as cylindrical ones, for example all the classic New Zealand examples from Matauri Bay show intermediate CP values (0.267-0.235) consistent with the presence of a significant proportion of both cylindrical and prismatic tubular forms, as are readily observed by SEM (Figures 2, 5). It would seem therefore that a further simplification and refinement of the classification of halloysite types recently summarized by Churchman (2015) into the four categories of tubular, platy, spheroidal and prismatic is called for. Thus rather than reserving the term prismatic for a distinct type of halloysite the tubular category should be subdivided into cylindrical and prismatic types, since the prismatic form is simply a common variant of the tubular form. Parenthetically, we note that none of the physical characteristics appear obviously correlated (Table 6) with the Fe content of the samples (Table 2). Presumably this reflects the fact that Fe may be present

in either minor impurity phases and/or incorporated in halloysites via isomorphous substitution, and elucidating the potential effects of Fe on halloysite will require more detailed investigation.

As far as the IR spectra are concerned, according to the review of Joussein et al., (2005), halloysite exhibits only two Al_2OH-stretching bands at 3695 and 3620 cm^{-1}. Our examination indicates that this is only the case for cylindrical tubular halloysites and that intermediate bands are evident in prismatic specimens, which based on additional tests, including formamide intercalation, show no obvious evidence for kaolinite as a separate phase. This is an important point because a physical mixture of halloysite and kaolinite could produce a similar IR pattern with apparent intermediate bands. Presumably the intermediate bands observed for prismatic halloysite are an indication of a generally more ordered pattern of hydrogen bonding of the layers, presumably a reflection of the fact that many layers are planar in the prismatic examples whereas in the cylindrical halloysites there is added disorder due to curvature of the layers which likely results in uncoupling of the surface OH bonds (Farmer, 1974). Additionally, the similarity of the IR spectra of prismatic forms of halloysite to those of kaolinite may be expected based on the observations of Kogure et al., (2013) that, locally, the stacking sequence in halloysite is identical to that of kaolinite. Although it is also noteworthy that heating cylindrical halloysite samples in the laboratory does not result in the appearance of intermediate OH stretching bands.

The measured 'OH stretching band intensity ratio' is also well correlated with the 'CP' index (Table 6) indicating that the features reflected in the XRD patterns of the halloysites are also reflected in the order/disorder of the hydrogen bonding of the layers

as revealed by IR spectroscopy. Remarkably this was noted almost 50 years ago by Chukhrov & Zvyagin (1966) and additionally by Bates (1971) who also went further and demonstrated that the ratio of the two main OH stretching adsorption bands was related to both the length and the order of halloysite tubes ('and laths'). These relationships with tube length and order are confirmed in the present study (Table 6), although it should be remarked that correlations to particle length are potentially subject to any prior processing that some of the beneficiated samples may have undergone, so it may be better practice to rely on correlations with particle diameter in order to assess the characteristics of such processed samples.

Returning to the structure of halloysite, peaks characteristic of the tendency towards the $2M_1$ stacking sequence ($\bar{1}12$, 021) in the terminology of Bailey (1990, 1993) were only observed in the XRD patterns of some prismatic samples all with 'CP' indices of < 0.26. However, these peaks were readily observed in the electron diffraction pattern collected from sample 14US, which by all other characteristics is a cylindrical example ('CP' index = 0.350). It is pertinent to note that Kohyama *et al*., (1978) also observed these peaks for a cylindrical tubular halloysite in both hydrated and dehydrated states by electron diffraction in a TEM equipped with an environmental cell. Chukhrov & Zvyagin (1966) also comment that the two layer structure was common to all halloysites when examined by electron diffraction regardless of the type of XRD pattern. Therefore, the electron diffraction evidence indicates that the same two layer stacking sequence or at least the tendency towards it is characteristic of both cylindrical and prismatic forms of halloysite. Presumably, it is only observed for cylindrical halloysites by electron diffraction because of the additional disorder due to curvature and the fact that electron

diffraction samples a smaller volume compared to powder XRD, which together with differences in scattering efficiency means that a material may be "X-ray amorphous", but at the same time "electron crystalline". Furthermore, in predominantly 10Å form the XRD patterns of some prismatic samples, notably 16US (see Figures 1 & 2 for images, 'CP' index = 0.186) and 17US (see Figure 5 for images 'CP' index = 0.213) examined in the present investigation, show an intense and sharp 021 peak at 4.35Å (Figures 6 & 7), along with the typical modulated 20,13 band. The presence of these features in the XRD patterns of the 10Å form of prismatic samples indicates that the $2M_1$ sequence or at least the tendency towards it and the flat prismatic faces and planar layers which produce the modulation of the 20,13 band must both be present prior to dehydration. The significance of these observations on cylindrical and prismatic forms is that together they argue against models that suggest that the planar faces of prismatic forms and the $2M_1$ layer stacking develop as a result of dehydration.

On the contrary, the evidence from determination of particle size distributions detailed above suggests that the prismatic tubular forms of halloysite are simply a late stage in a natural growth sequence of tubular form that evolves from cylindrical to prismatic as tube size increases (Figure 13). If so, then an alternative explanation to dehydration for a change from cylindrical to polygonal prismatic morphology is required. For this we turn to the original work of Bates *et al*., (1950) who pointed out that the mechanism of alleviating the misfit of tetrahedral and octahedral sheets by curvature of the layers has an ideal radius of curvature. Bailey (1990) updated the calculations of Bates *et al*., (1950) and determined values of 198.9 Å for the inner tube diameter, if the crystallographic b axis is parallel to the tube axis, which is usually the case, and 149.1 Å

if the tube axis is parallel to a. At either smaller or greater diameters the mechanism of misfit accommodation by curvature must necessarily subject the structure to increasing strain. The issue with smaller values has been suggested to explain why halloysite forms as hollow tubes, and here we suggest that a similar issue with larger radii of curvature may be a simple explanation of why in larger diameter tubes curved layers give way to polygonal radial sectors in which the layers adopt a planar form. Hence as the tubes grow larger it is no longer energetically favorable to compensate misfit between tetrahedral and octahedral sheets by curvature and at so at some critical radius other mechanisms common in phyllosilicates generally, such as tetrahedral rotation, presumably come into play. Consequently, the layers switch from a curved to a planar arrangement such that prismatic tubular forms may be seen as the result of a natural structural progression of tube growth to sizes beyond which the lateral misfit is not comfortably accommodated by curvature. We assume that once a layer becomes flattened around the circumference of the tube, subsequent layer growth is also in planar layers and so proliferates the pattern and in so doing builds up a structure of radial sectors. In terms of layer arrangement there is obvious analogy with polygonal or so called 'Povlen' serpentine which has been studied in much greater detail than halloysite by high resolution TEM, see for example Baronnet & Devouard (1996). Indeed, polygonal serpentine is usually noted as being much larger in diameter than associated cylindrical chrysotile, which has also been shown to occur in the core of the larger polygonal forms. We speculate that a similar such arrangement i.e. cores of curved layers may be a common feature of prismatic halloysite, in fact the cross section shown in Figure 3c of Kogure et al., (2013) could be an example of this arrangement, as illustrated

schematically in Figure 13. It is also tempting to speculate that the spindle like structures (Figure 5) often noted in prismatic halloysites (Dixon & McKee, 1974) and the 'extrusion' of the spindles as a result of sample preparation procedures as described by Chukhrov & Zvyagin (1966), may be a result of a zone of weakness in the particles at the point where a cylindrical arrangement of layers transitions to a planar prismatic one. Additionally, observations in the early literature that 'metahalloysite' tended to show more order and therefore that fully hydrated forms of halloysite were more likely to be cylindrical tubes is suggestive of a greater propensity for prismatic forms to dehydrate, which we postulate may be related to the change in the mechanism to accommodate the octahedral to tetrahedral misfit and its effect on the environment of interlayer H_2O molecules.

The correlations of both the XRD 'CP' index and the IR 'OH stretching band intensity ratio' with surface area determined by N_2 adsorption (Table 6) indicate that measured surface area is also related to the proportions of cylindrical versus prismatic tubes in any given halloysite sample. This may be explained as a consequence of the underlying relationships between morphology/order and size characteristics. In addition to these relationships the other clear difference between samples was in relation to the presence or absence of hysteresis in the adsorption/desorption isotherms and when present the extent of hysteresis is also well correlated with the 'CP' and 'OH stretching band intensity ratio'. Churchman et al., (1995) also demonstrated that some samples of halloysite showed hysteresis whilst other samples showed little or none. They noted that hysteresis was shown by halloysites that consisted of the smallest particles (diameters <0.08 μm) as measured by TEM. In terms of an explanation, tentatively we suggest that

hysteresis may be related to the presence of slit shaped pores between bundles of cylindrical tubes, which is typically the form of the smallest halloysite tubes, such an origin would account for its absence in samples of largely prismatic form because these forms may pack together more closely due to the predominance of flat rather than curved surfaces. Thus although hysteresis tends to be positively correlated with surface area, samples exist with relatively high surface area such as sample 1Au (62.6 m^2g^{-1}), which due to predominantly prismatic form, shows only a relatively small amount of hysteresis. Apart from the fact that cylindrical halloysites tend to have much higher specific pore volumes detailed porosity characteristics may be more difficult to predict, perhaps because a variety of other pore types may be present within and between packets of layers within both cylindrical and prismatic types (Dixon & McKee, 1974; Churchman et al., 1995).

CONCLUSIONS

The mineralogical and the physical characteristics of tubular halloysites are interrelated. Features of the XRD patterns and IR spectra of halloysite samples can be directly related to the proportions of cylindrical versus prismatic tubular forms. Cylindrical forms of halloysite are typically smaller in both diameter and length than prismatic forms and consequently characteristics such as specific surface area and CEC can also be anticipated from the character of halloysite XRD patterns and IR spectra. Prismatic halloysite is not a rare form but a common morphology found in many samples. The relationships between form and size characteristics suggest that the prismatic morphology

is formed as a natural consequence of continued tube growth rather than as a result of dehydration (Figure 13).

In terms of the many technological applications being investigated and proposed for tubular halloysites different samples of halloysite may vary considerably in their relevant characteristics and identifying the optimum type for a given application, as emphasized by Pasbakhsh et al., (2013) may be key to success or failure. The relationships demonstrated herein should enable the physical characteristics of halloysites to be more readily assessed and understood within the wider context of their natural variation and choices in relation to tailoring of properties to applications and issues of quality control more easily made and assessed.

ACKNOWLEDGEMENTS

Angie Main is acknowledged for recording many of the infrared spectra. We thank Andre Zeitoun (Applied Minerals) for provision of access to samples from the Dragon Mine, and Jeremy Hooper and John Keeling for samples from Imerys and Australia, respectively. Support of the Scottish Government's Rural and Environment Science and Analytical Services (RESAS) Division is gratefully acknowledged. TEM data was enabled via support from the EPSRC-funded Leeds EPSRC Nanoscience and Nanotechnology Equipment Facility (LENNF) (EP/K023853/1). We also gratefully acknowledge the helpful and constructive reviews of Paul Schroeder, an anonymous reviewer, and the editorial comments of Jock Churchman.

REFERENCES

Bailey S.W. (1980) Summary of recommendations of AIPEA nomenclature committee. *Clay Minerals*, **15**, 85-93.

Bailey S.W. (1990) Halloysite: a critical assessment. Pp. 89-98 in: *Proceedings of the 9th International Clay Conference 1989* (V.C. Farmer & Y. Tardy, editors). Sciences Géologiques, Mémoire 86, Strasbourg, France

Bailey SW. (1993) Review of the structural relationships of the kaolin minerals. Pp. 25-42 in: *Kaolin genesis and utilization*. (H.H. Murray, W.M. Bundy & C.C. Harvey, editors). Boulder, CO: The Clay Minerals Society.

Baronnet A. & Devouard B. (1996) Topology and crystal growth of natural chrysotile and polygonal serpentine. *Journal of Crystal Growth*, **166**, 952-960.

Bates T. F. (1971) The kaolin minerals. Pp. 109-157 in: *The Electron Optical Investigation of Clays* (J.A. Gard, editor). Mineralogical Society, London.

Bates T.F., Hildebrand F.A. & Swineford A. (1950) Morphology and structure of endellite and halloysite. *American Mineralogist*, **35**, 463-484.

Bates T.F. & Comer J.J. (1957) Further observations on the morphology of chrysotile and halloysite. *Clays and Clay Minerals*, **6**, 237-248.

Brindley G.W. (1984) Order-disorder in clay mineral structures. Pp. 125-196 in: *Crystal Structures of Clay Minerals and their X-ray Identification* (G.W. Brindley & G. Brown, editors). Mineralogical Society, London, UK.

Brindley G.W. & Robinson K. (1948) X-ray studies of halloysite and metahalloysite. *Mineralogical Magazine*, **28**, 393-406.

Brindley G.W., de Souza Santos P. & de Souza Santos H. (1963) Mineralogical studies of kaolinite-halloysite clays: Part I. Identification problems. *American Mineralogist*, **48**, 897-910.

Chukhrov F. V. & Zvyagin B. B. (1966) Halloysite, a crystallochemically and mineralogically distinct species: Pp. 11-25 in: *Proceedings of the International Clay Conference Jerusalem, Israel.* (L. Heller & A. Weiss, editors). Israel Program for Scientific Translation, Jerusalem, Israel.

Churchman G.J. (2015) The identification and nomenclature of halloysite (a historical perspective). Pp. 51-67 in: *Natural Mineral Nanotubes* (P. Pasbakhsh & G.J. Churchman, editors). Apple Academic Press, Oakville, Canada.

Churchman G.J. & Carr R.M. (1975) The definition and nomenclature of halloysites . *Clays and Clay Minerals*, **23**, 382-388.

Churchman G.J., Whitton J.S., Claridge G.G.C. & Theng B.K.G. (1984) Intercalation method using formamide for differentiating halloysite from kaolinite. *Clays and Clay Minerals*, **32**, 241-248.

Churchman G.J., Davy T.J., Aylmore L.A.G., Gilkes R.J. & Self P.G. (1995) Characteristics of fine pores in some halloysites. *Clay Minerals*, **30**, 89-98.

Costanzo P. M., Giese R. F., & Lipsicas M. (1984) Static and dynamic structure of water in hydrated kaolinites; I, The static structure. *Clays and Clay Minerals*, **32**, 419-128.

de Souza Santos P., Brindley G.W. & de Souza Santos H. (1965) Mineralogical studies of kaolinite-halloysite clays: part III. A fibrous kaolin mineral from Piedade, Säo Paulo, Brazil. *American Mineralogist*, **50**, 619-628.

Dixon J.B. (1989) Kaolin and Serpentine Group Minerals. Pp. 467 525 in: *Minerals in Soil Environments* (J.B. Dixon & S.B. Weed, editors). Soil Science Society of America, Madison, Wisconsin.

Dixon J.B. & McKee, T.R. (1974) Internal and external morphology of tubular and spheroidal halloysite particles. *Clays and Clay Minerals*, **22**, 127–137.

Ece Ö. I & Schroeder P.A. (2007) Hydrothermal Alteration of Oligocene volcanic rocks and genesis of hallyosite-alunite-kaolinite deposits in the Turplu area, Balikesir, Turkey. *Clays and Clay Minerals*, **55**, 18-36.

Farmer V.C. (1974) The layer silicates. Pp. 331-363 in: *The infrared spectra of minerals*. IR spectra. (V.C. Farmer, editor). Mineralogical Society, London, UK.

Giese R.F. Jr (1988) Kaolin minerals structures and stabilities. Pp 29-66, In: *Hydrous phyllosilicates (exclusive of micas)* (S.W. Bailey editor) Reviews in Mineralogy 19, Mineralogical Society of America.

Gray N., Lumsdon D.G. & Hillier S. (submitted) Effect of pH on the cation exchange capacity of some tubular halloysites (HNT's). *Clay Minerals*.

Heddle Prof. (1882) Minerals new to Britain. *Mineralogical Magazine*. **5**, A-2.

Hillier S. (1999) Use of an air brush to spray dry samples for X-ray powder diffraction. *Clay Minerals*, **34**, 127-135.

Hillier S. & Ryan P.C. (2002) Identification of halloysite (7 angstrom) by ethylene glycol solvation: the 'MacEwan effect'. *Clay Minerals*, **37**, 487-496.

Hoffman U., Morcos S. & Schembra F.W. (1962) Das sonderbarste Tonmineral, der halloysite. *Berichte der Deutschen Keramischen Gesellschaft*, **39**, 474-482.

Honjo G., Kitamura N & Mihama K. (1954) A study of clay minerals by means of single-crystal electron diffraction diagrams - the structure of tubular kaolin. *Clay Minerals Bulletin*, **4**, 133-141.

Joussein E., Petit S., Churchman J., Theng B., Righi D. & Delvaux B. (2005) Halloysite clay minerals- a review. *Clay Minerals*, **40**, 383-426.

Keeling, J., Pasbakhsh, P. & Churchman, G.J. (2011). Halloysite from the Eucla Basin, South Australia - comparison of physical properties for potential new uses. Pp. 351–359 in: *10th International Congress for Applied Mineralogy (ICAM)*. (*M.* Broekmans, editor) Trondheim, Norway.

Kogure T., Mori K., Drits V.A. & Takai Y. (2013) Structure of prismatic halloysite. *American Mineralogist*, **98**, 1008–1016.

Kohyama N., Fukushima K. & Fukami A. (1978) Observation of the hydrated form of tubular halloysite by an electron microscope equipped with an environmental cell. *Clays and Clay Minerals*, **26**, 25-40.

Limpert E., Stahel W., & Abbt M., (2001) Log-normal Distributions across the Sciences: Keys and Clues. *BioScience*, **51**, 341–352.

Norrish K. (1995) An unusual fibrous halloysite. Pp. 275–284 in: *Clays Controlling the Environment*. Proceedings of the 10th International Clay Conference, Adelaide 1993 (G.J. Churchman, R.W Fitzpatrick & R.A. Eggleton, editors). CSIRO Publishing, Melbourne, Australia.

Omotoso O., McCarty D.K., Hillier S. & Kleeberg R. (2006) Some successful approaches to quantitative mineral analysis as revealed by the 3rd Reynolds Cup Contest. *Clays and Clay Minerals*, **54**, 748-760.

Pasbakhsh P., Churchman G.J. & Keeling J.L. (2013). Characterisation of properties of various halloysites relevant to their use as nanotubes and microfibre fillers. *Applied Clay Science*, **74**, 47-57.

RasbandW.S. (1997-2015) ImageJ, U. S. National Institutes of Health, Bethesda, Maryland, USA, http://imagej.nih.gov/ij/, 1997-2015.

Singh B. (1996) Why does halloysite roll? – A new model. *Clays and Clay Minerals*, **44**, 191-196.

Ünal-Ercan H., Ece Ö. I., Schroeder P.A. & Karacik Z. (2016) Differentiating styles of alteration within kaolin-alunite hydrothermal deposits of Canakkale, Turkey. *Clays and Clay Minerals* (in review)

Wilson I.R. (2004) Kaolin and halloysite deposits of China. *Clay Minerals*, **39**, 1-15.

Wilson I. R. & Keeling J.L. (submitted) Global occurrence and geology of halloysite. *Clay Minerals*.

List of Figures

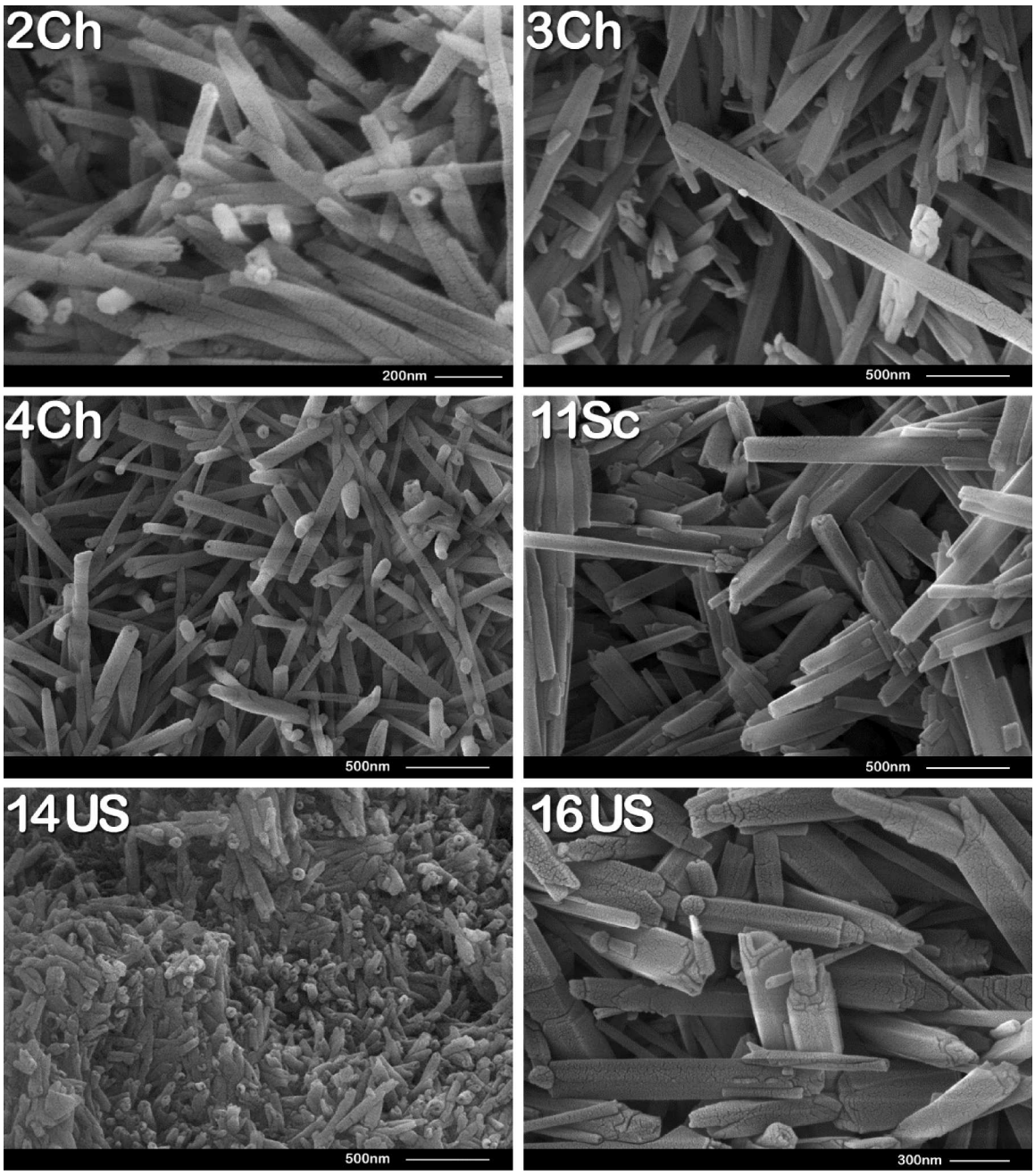

Figure 1. SEM images of cylindrical and prismatic tubular morphology. Samples 2Ch, 4Ch, and 14US show mainly cylindrical forms, samples 3Ch, 11Sc, and 16US show mainly prismatic forms, although some cylindrical tubes are also apparent in sample 3Ch. Cylindrical tubes show smaller diameters than prismatic ones.

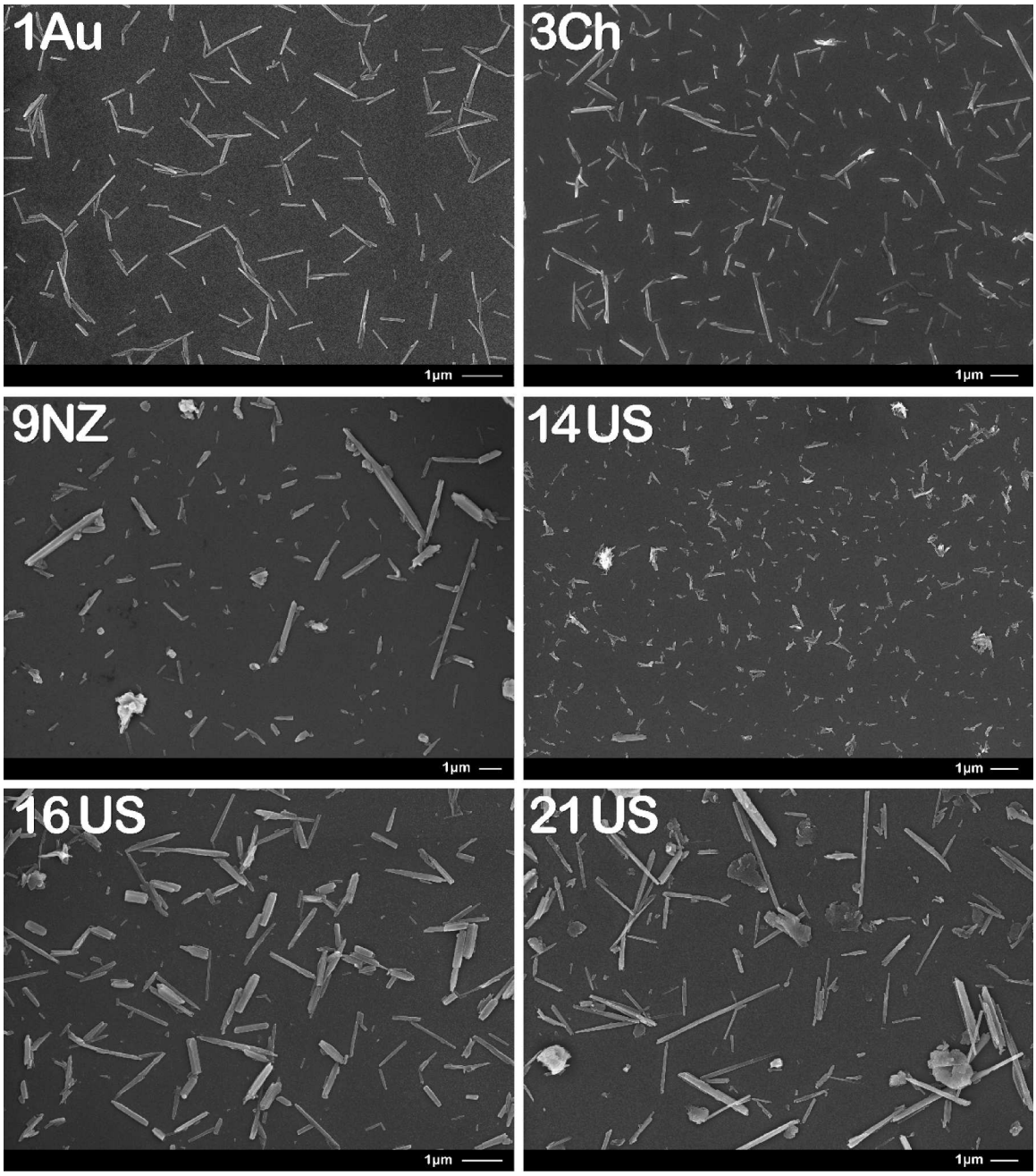

Figure 2. Examples of dispersed halloysite samples 1Au, 3Ch, 9NZ, 14US, 16US, and 21US prepared for measurement of particle length and diameter by image analysis. Note variation in size of 1 micrometer scale bars.

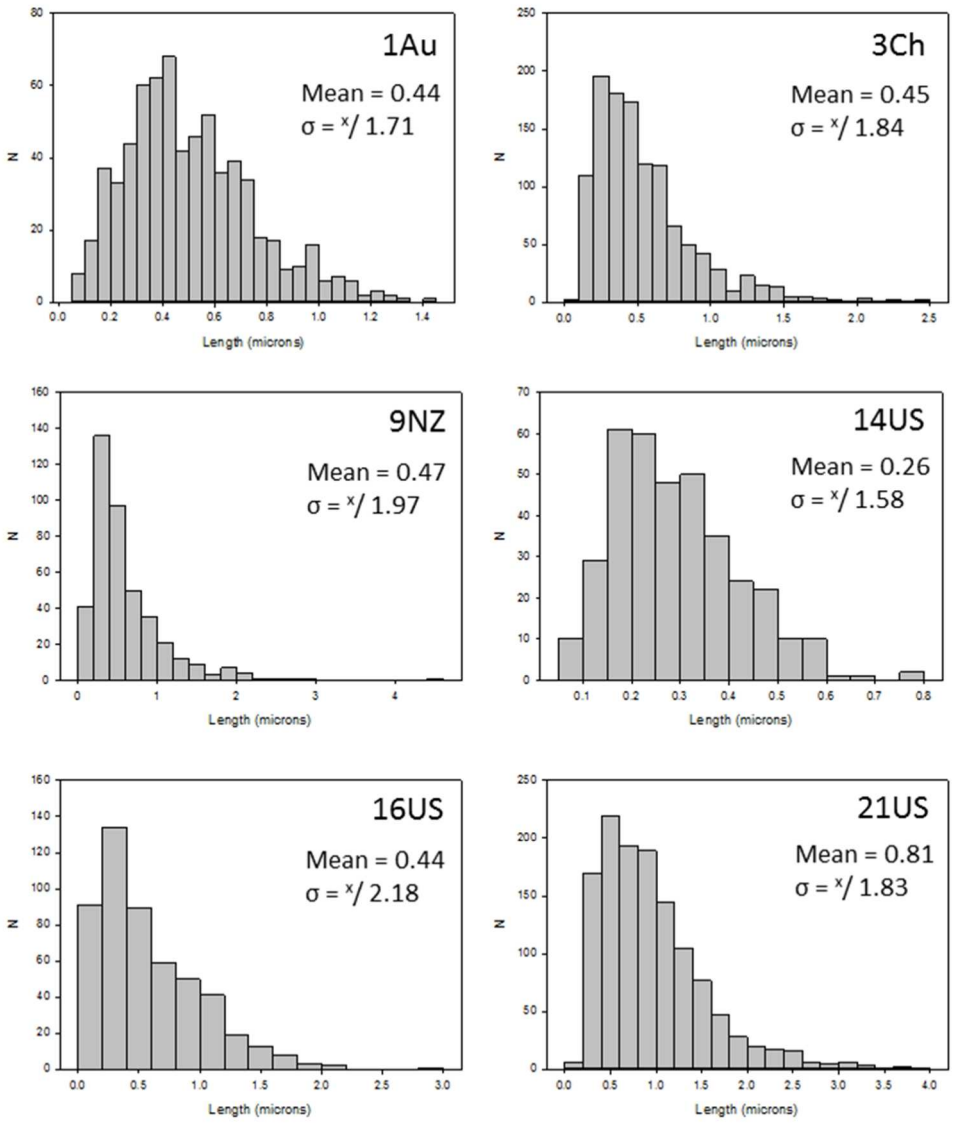

Figure 3. Examples of particle size distribution histograms with respect to tube length. Samples correspond to those for which example images are shown in Figure 2. Note standard deviations are indicated as multiply or dividing the mean value to describe the distribution about it.

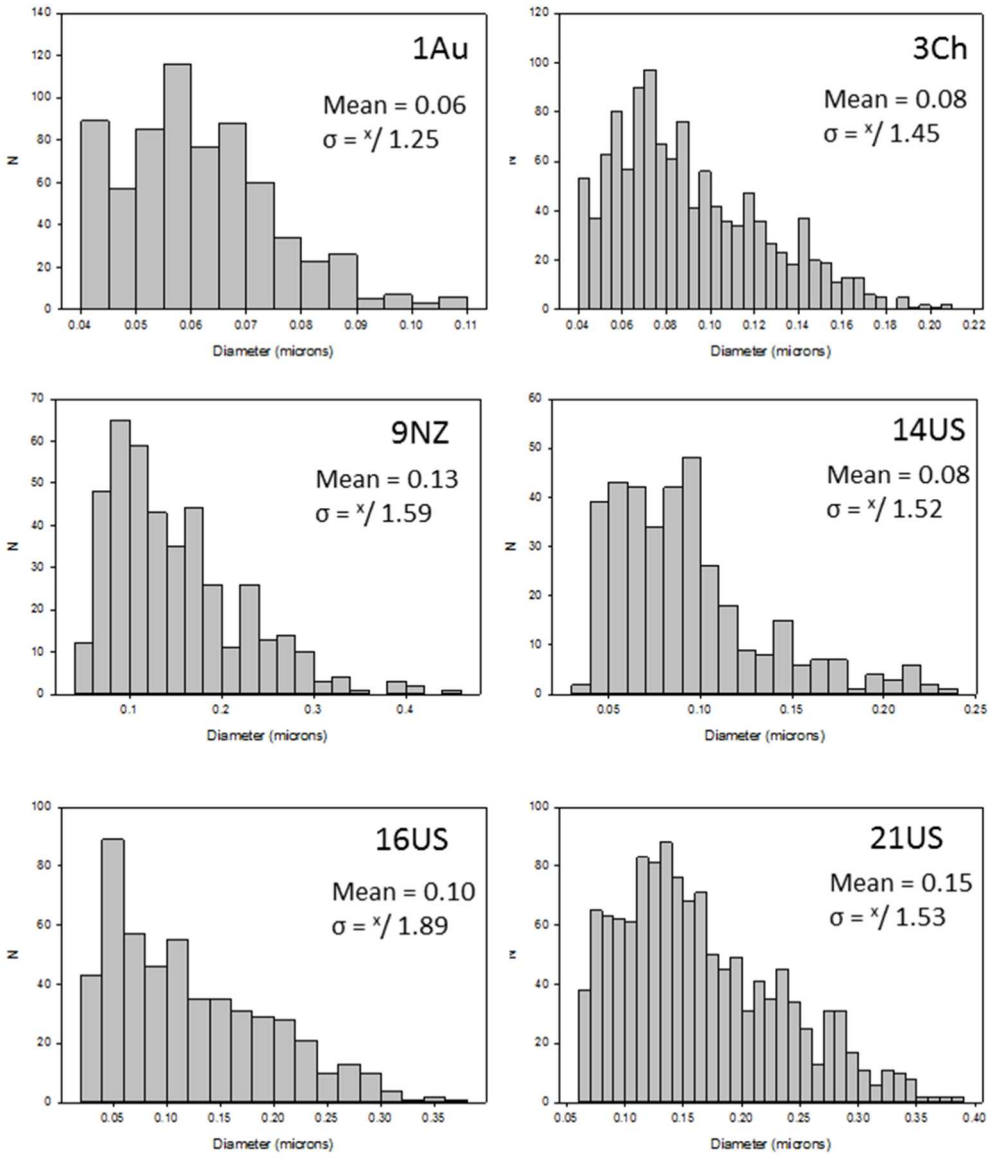

Figure 4. Examples of particle size distribution histograms with respect to tube diameter. Samples correspond to those for which example images are shown in Figure 2. Note standard deviations are indicated as multiply or dividing the mean value to describe the distribution about it.

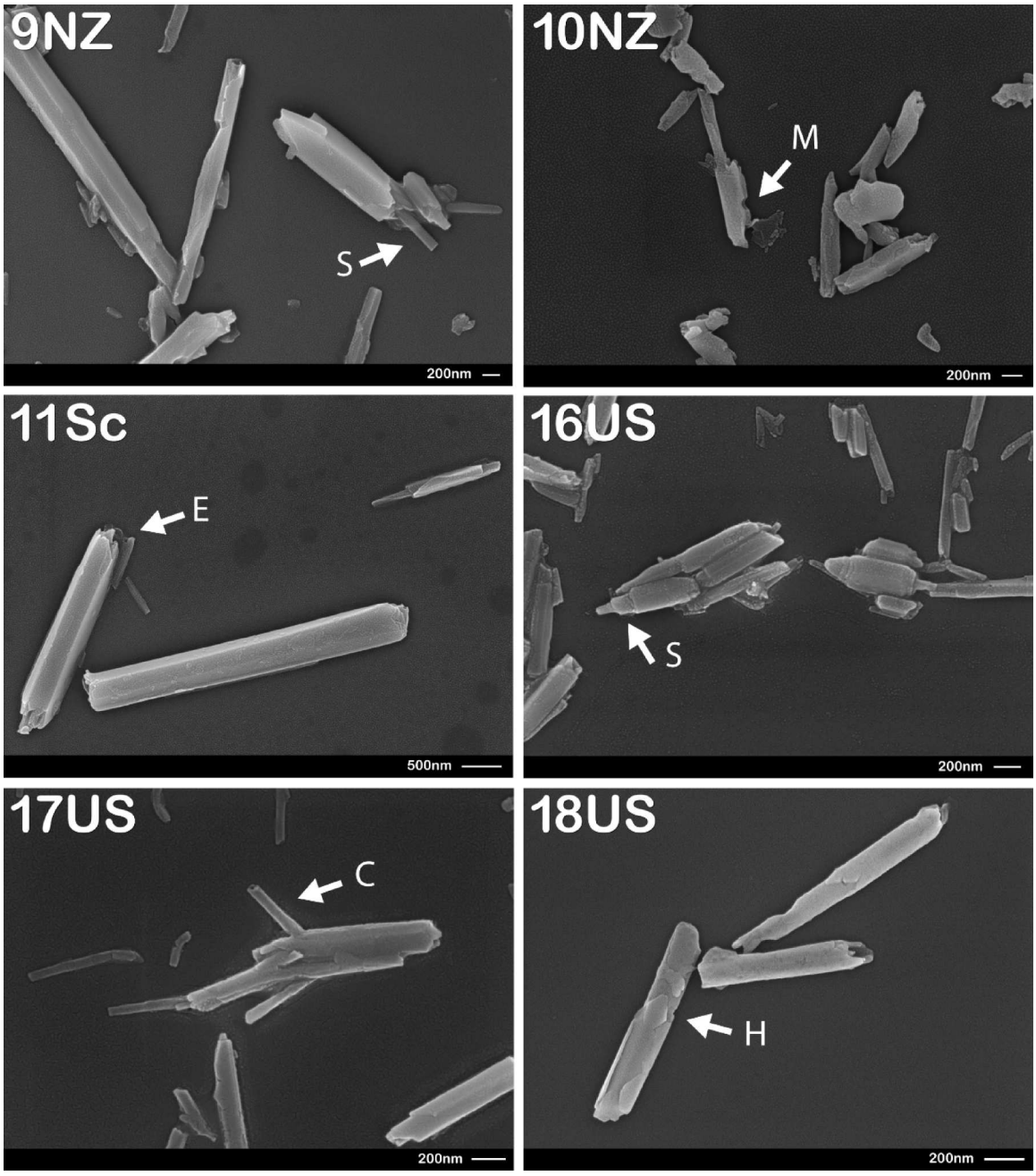

Figure 5. Example of particle morphologies in high magnification images of dispersed samples. Note 'serrated' tube end edges of some prismatic tubes (e.g. 'E' in 11Sc), 'spindle' like morphologies (e.g. 'S' in 9NZ & 16US), hexagonal outlines on some particle surfaces (e.g. 'H' in 18US) intersection mould ('M' in prismatic particle near center of image in 10NZ), and cylindrical nature of smaller intersecting tubes (e.g. 'C' in 17US). Note variation in size of scale bars.

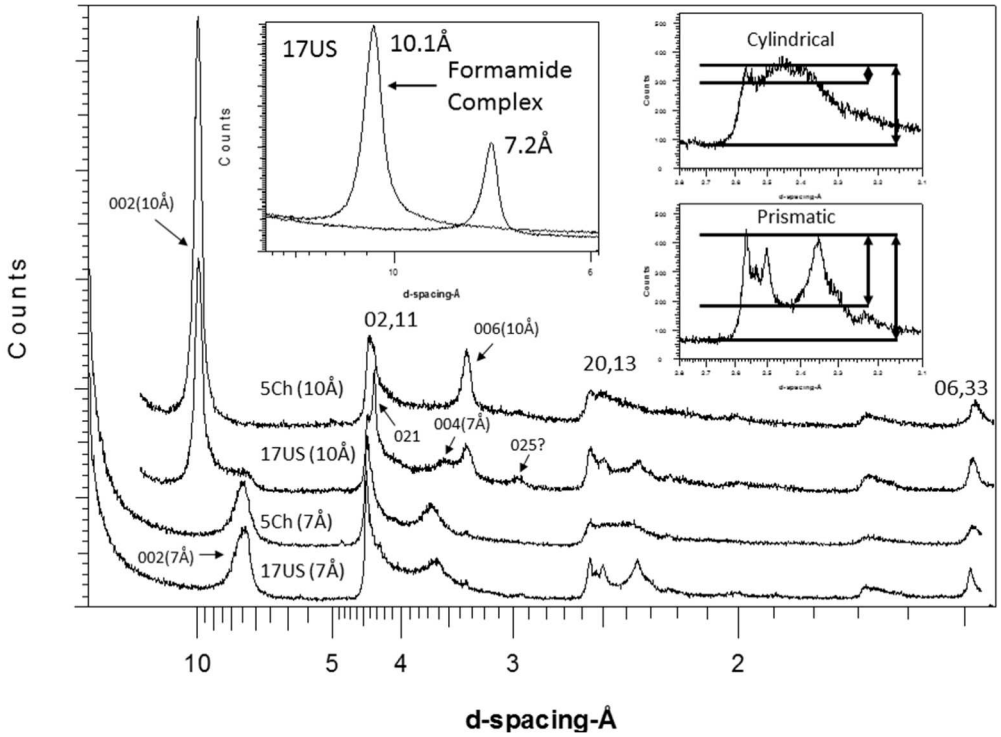

Figure 6. Examples of random powder patterns of cylindrical (5Ch) and prismatic (17US) tubular forms of halloysite in both 10Å and 7Å form. Inserts illustrate measurement of the cylindrical/prismatic 'CP' index from the 02,13 diffraction band, and reaction of sample 17US to treatment with formamide, which confirms the absence of kaolinite in this sample. Note the peak near 4.35Å in the (predominantly) 10Å form of sample 17US, which is taken as the 021 peak. Because 17US is not entirely 10Å, the broad peak near 3.5Å is taken as the 004 compared to the 10Å form of 5Ch which only shows the 10Å 006 near 3.35Å. The smaller peak near 3Å in 17US is possibly 025. Indices assume a 2 layer structure.

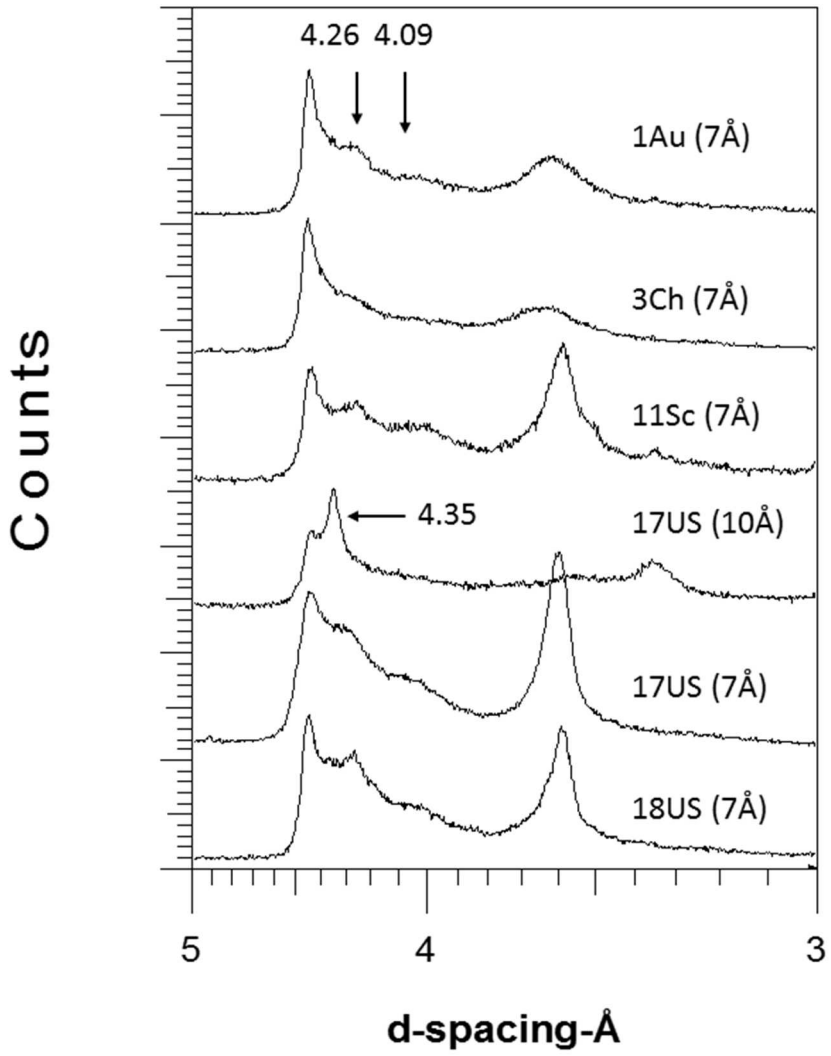

Figure 7. Examples of diffraction patterns of the 02, 11 band of several prismatic samples all showing evidence of 021 and T12 peaks in the tail of the band. All samples are in the 7Å dehydrated form except sample 17US which is shown in both dehydrated (7 Å) and hydrated (10 Å) form. In 10Å form the 021 peak is at 4.35 Å.

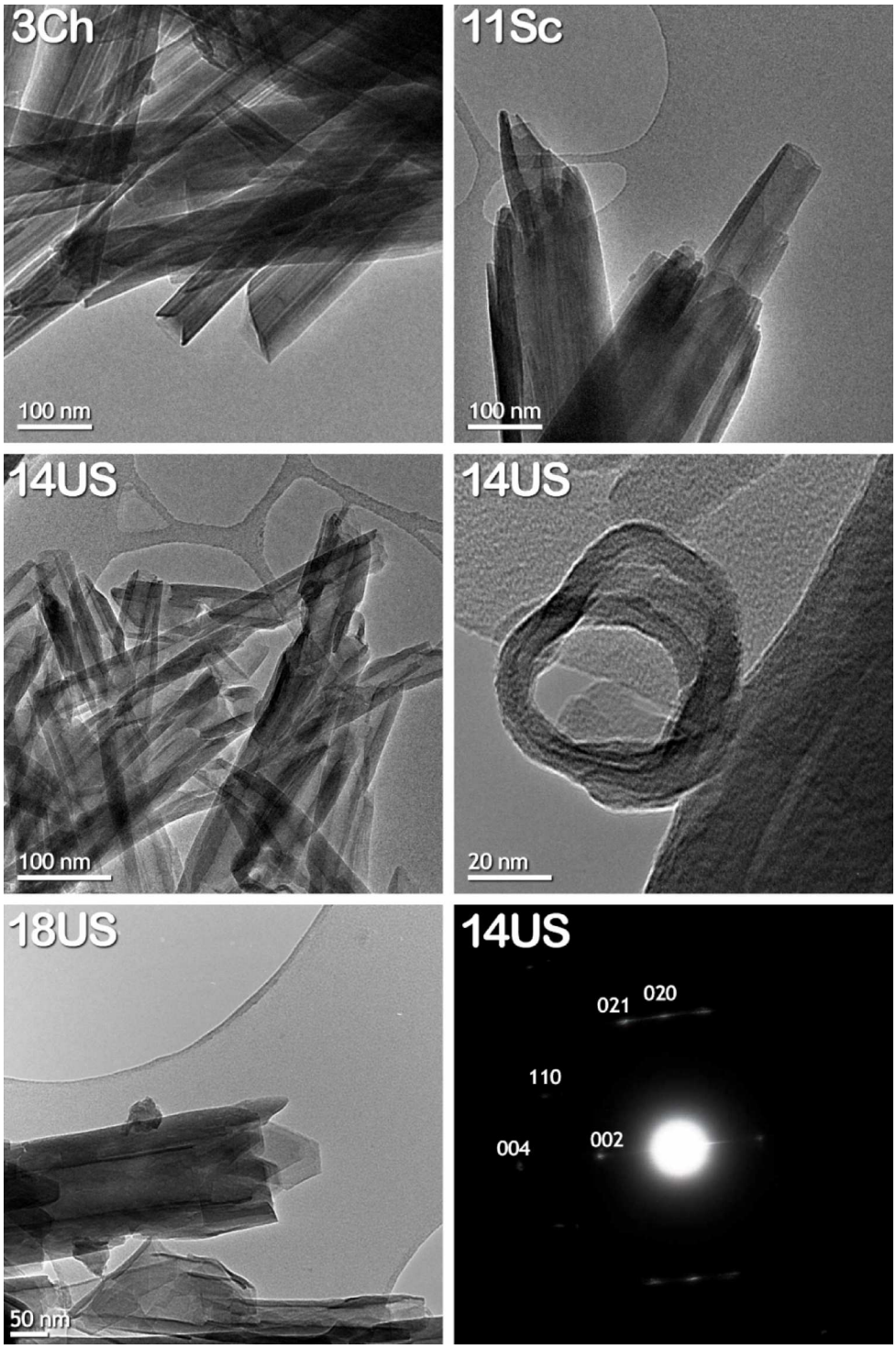

Figure 8. TEM images of selected samples showing electron transparent lumens in both cylindrical (14 US) and prismatic types (3Ch, 11Sc, 18US). Note details of tube endings. Also shown is an electron diffraction pattern from a cylindrical tube in sample 14US, which is consistent with the two layer structure reported by earlier workers.

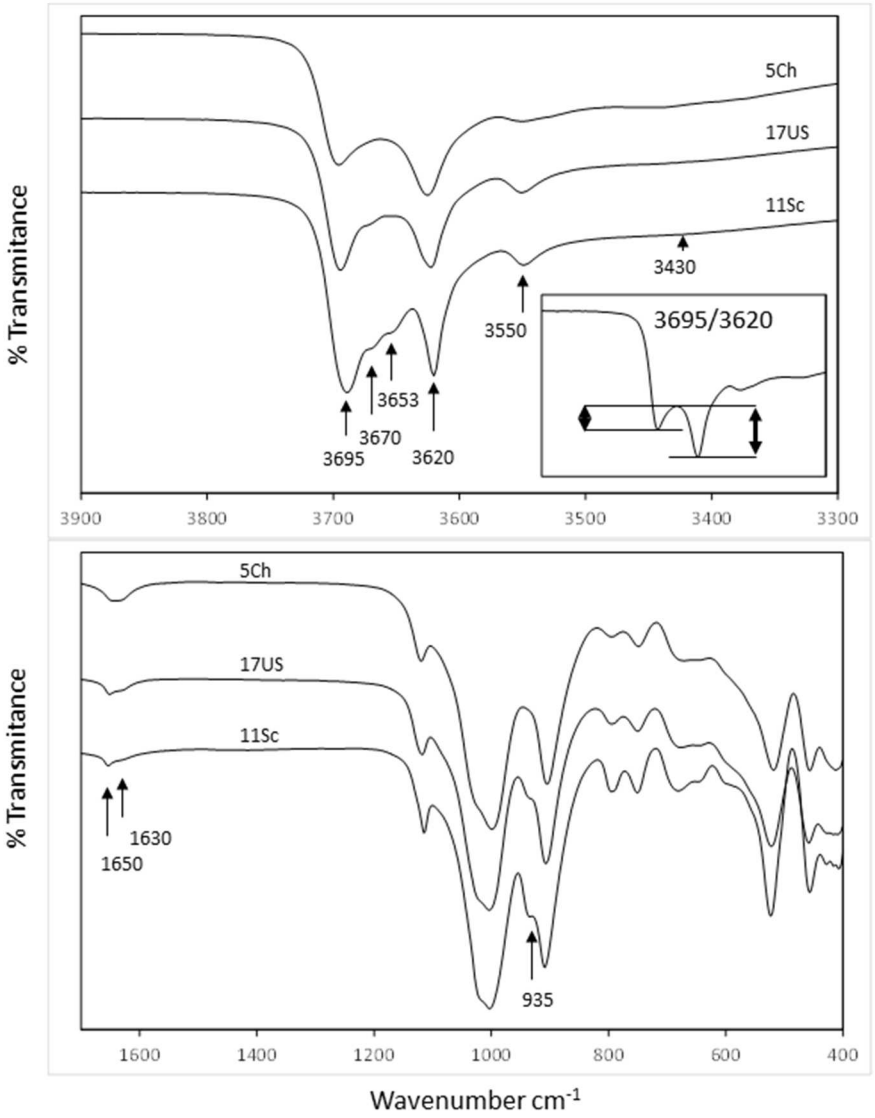

Figure 9. Examples of infrared spectra of cylindrical (5Ch) and prismatic forms (17US, 11SC) of halloysite. Insert illustrates the measurement of the 'OH stretching band ratio'.

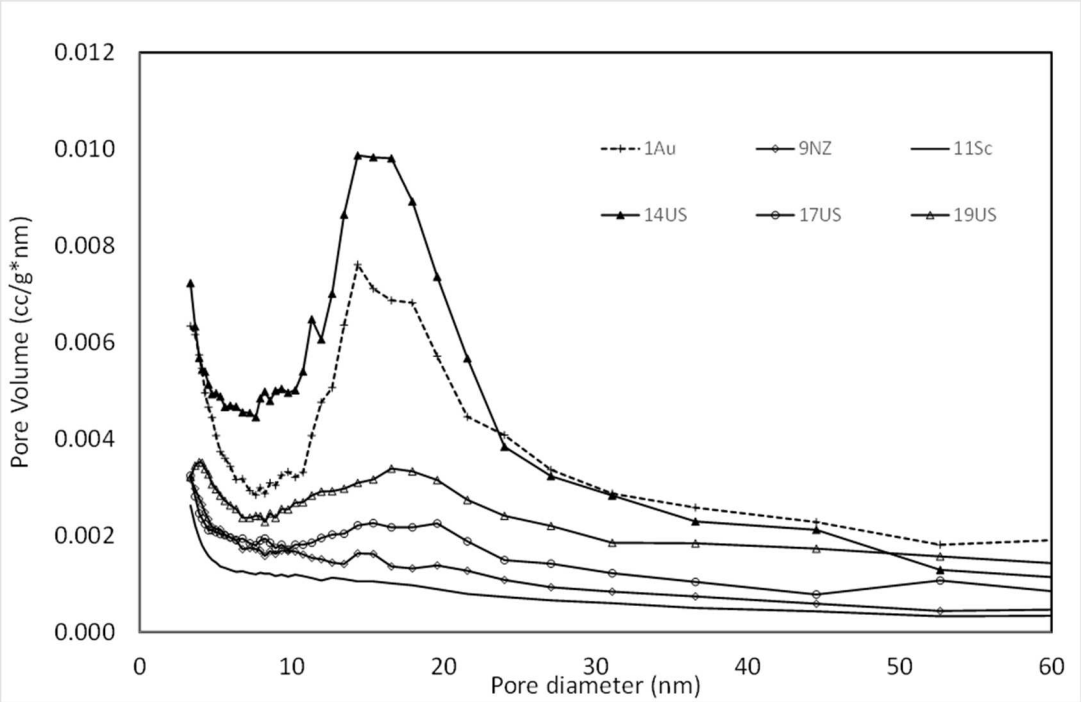

Figure 10. Examples of differential pore volume plots. The peaks in the distributions near 17 nm are assumed to correspond to the central lumen of the tubes. Isotherms for the same six samples are shown in Figure 11.

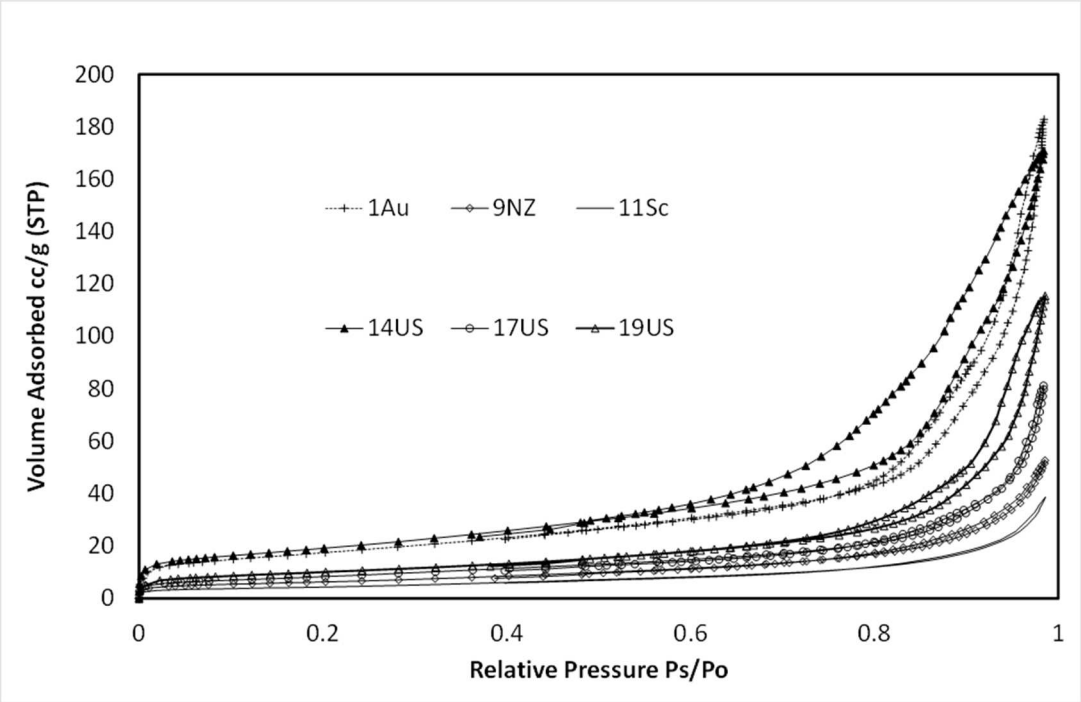

Figure 11. Examples of the N_2 adsorption and desorption isotherms for cylindrical and prismatic forms of halloysite. Cylindrical forms show obvious hysteresis. Differential pore volume plots for the same six samples are shown in Figure 10.

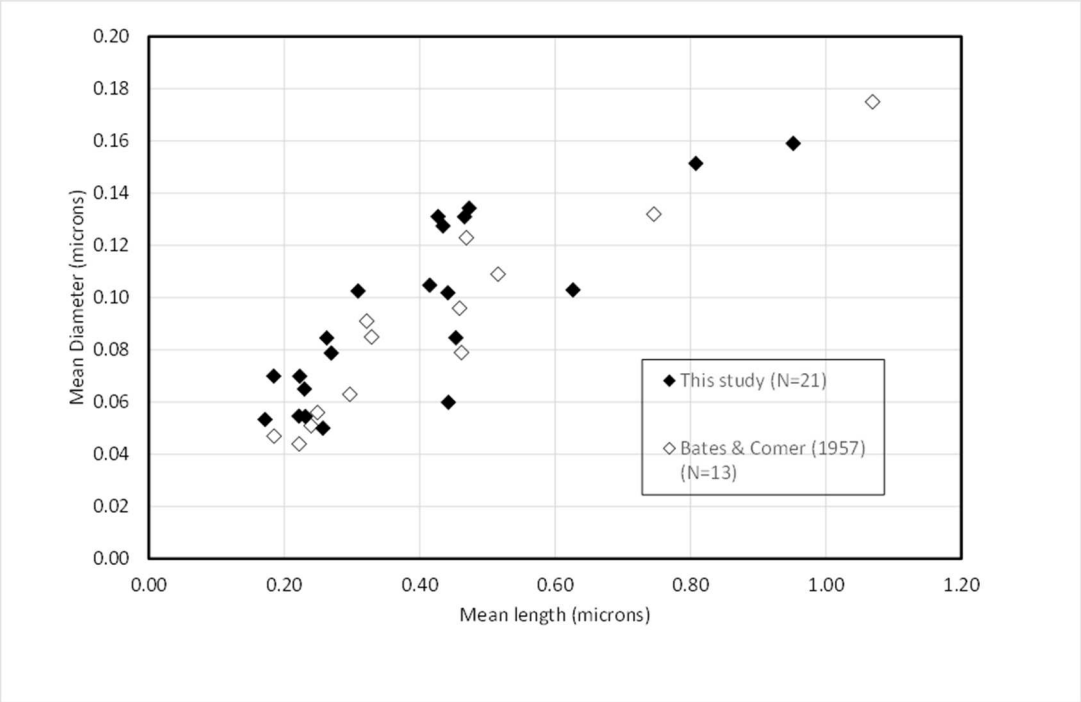

Figure 12 Mean length versus mean diameter for the studied samples plotted along with data from Bates & Comer (1957) which show comparable relationships.

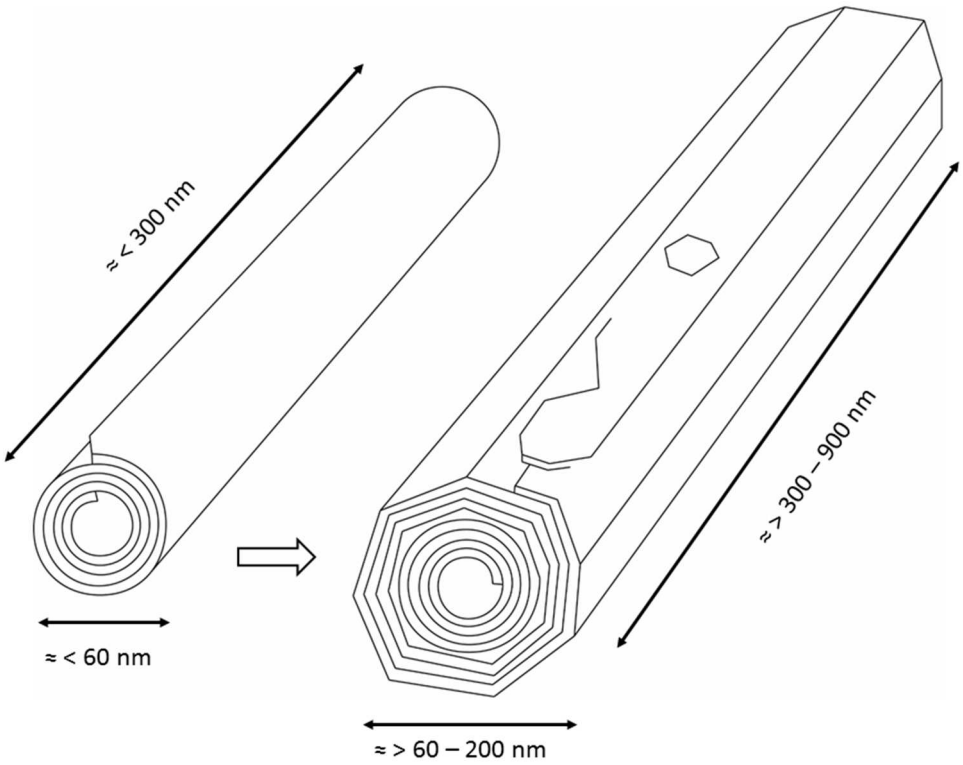

Figure 13. Proposed relationship of cylindrical and prismatic tubular halloysites in hydrated form and structure in cross section. Prismatic tubes are formed by continued growth of cylindrical forms. Typical mean diameters and lengths are indicated. Large prismatic tubes often show hexagonal outlines on their surfaces, which may represent epitaxial kaolinite, e.g. as imaged in sample US18 (Figure 5).

Table 1. Origin and provenance of halloysite samples investigated.

Sample	Country	Location	Source of Samples
1Au	Australia	Ecula Basin, S. Australia	John Keeling
2Ch	China	Zunyi region, Guizhou Province	Ian Wilson
3Ch	'	Dafang region, Guizhou Province	'
4Ch	'	'	'
5Ch	'	Bifa deposit, Yunnan Province	'
6Ch	'	Wan Jiar depoist, Yunnan Province	'
7Ch	'	Unknown location	IMERYS
8NZ	New Zealand	Matauri Bay, North Island	'
9NZ	'	'	Jock Churchman
10NZ	'	'	Unknown
11Sc	Scotland	Hospital Quarry, Elgin, Scotland	Heddles halloysite
12Tu	Turkey	Unknown location	IMERYS
13Tu	'	Balikesir region	Unknown
14US	USA	Dragon Mine, Utah	Applied Minerals. Inc
15US	'	'	'
16US	'	'	'
17US	'	'	'
18US	'	'	'
19US	'	Dragon Mine, Utah	IMERYS
20US	'	Dragon Mine, Utah	Sigma Aldrich, Lot No MKBQ2512V
21US	'	Bovill deposit, Idaho	Iminerals Inc

Table 2. Chemical composition of the samples made by XRF. All data normalised to theoretical kaolinite basis (86 wt.%) which is also shown for comparison. Note that elements beyond Si and Al may occur variably as isomorphous substitutions (e.g. Fe), exchangeable cations (e.g. Mg, Ca, K, Na) or in associated impurities.

Sample	SiO_2	Al_2O_3	TiO_2	Fe_2O_3	Mn_3O_4	MgO	CaO	K_2O	Na_2O
1Au	45.91	38.91	0.09	0.86	0.00	0.17	0.00	0.09	0.00
2Ch	47.37	37.97	0.05	0.41	0.01	0.03	0.18	0.03	0.00
3Ch	46.60	39.37	0.00	0.05	0.00	0.00	0.02	0.00	0.00
4Ch	45.77	39.63	0.01	0.09	0.02	0.09	0.25	0.03	0.15
5Ch	45.33	39.87	0.07	0.34	0.00	0.05	0.17	0.20	0.00
6Ch	45.93	39.89	0.00	0.11	0.00	0.00	0.11	0.00	0.00
7Ch	46.39	39.15	0.00	0.28	0.01	0.04	0.13	0.04	0.00
8NZ	47.24	38.20	0.10	0.40	0.00	0.08	0.01	0.00	0.00
9NZ	48.20	37.43	0.09	0.25	0.00	0.00	0.00	0.00	0.07
10NZ	50.13	35.52	0.07	0.26	0.00	0.00	0.07	0.00	0.00
11Sc	45.81	36.16	0.19	3.02	0.00	0.23	0.13	0.48	0.02
12Tu	44.97	39.25	0.20	1.12	0.00	0.09	0.12	0.30	0.00
13Tu	46.92	38.32	0.04	0.64	0.00	0.05	0.06	0.02	0.00
14US	46.39	39.43	0.00	0.10	0.00	0.07	0.09	0.00	0.00
15US	46.05	39.75	0.00	0.07	0.00	0.05	0.13	0.00	0.00
16US	45.78	37.55	0.10	2.52	0.00	0.00	0.09	0.00	0.00
17US	46.23	39.08	0.00	0.43	0.00	0.08	0.22	0.00	0.00
18US	45.58	39.93	0.00	0.00	0.00	0.34	0.11	0.03	0.05
19US	46.26	39.07	0.02	0.51	0.00	0.02	0.16	0.00	0.00
20US	45.73	39.60	0.01	0.22	0.01	0.07	0.36	0.04	0.02
21US	48.81	35.46	0.14	0.95	0.02	0.16	0.23	0.22	0.05
Kaolinite	46.55	39.50	0.00	0.00	0.00	0.00	0.00	0.00	0.00

Table 3. Size data for the samples obtained by manual measurement (maximum and minimum lengths and diameters values) and by image analysis (median and mean). Also listed are skewness, aspect ratios and calculated specific surface areas. Standard deviations should be understood as multiplying or dividing (X/) the mean values.

Sample	Max L	Max D	Min L	Min D	Skew	Med L	Med D	Med AR	Mean L	σ	Mean D	σ	Mean AR	σ	AR10%	N particles	$SAm^2g^{-1}_{calc}$
1Au	1.82	0.11	0.07	0.04	0.75	0.46	0.06	7.8	0.44	1.71	0.06	1.25	7.4	1.59	15.3	676	84.1
2Ch	1.49	0.10	0.06	0.03	1.07	0.25	0.05	4.7	0.23	1.60	0.05	1.31	4.2	1.58	8.9	209	96.6
3Ch	5.10	0.25	0.13	0.04	1.76	0.46	0.08	5.4	0.45	1.84	0.08	1.45	5.4	1.64	13.2	1176	44.0
4Ch	1.87	0.18	0.07	0.03	2.17	0.22	0.07	3.6	0.23	1.82	0.07	1.46	3.5	1.70	9.7	911	63.9
5Ch	1.38	0.14	0.09	0.02	1.52	0.25	0.05	5.0	0.26	1.71	0.05	1.49	5.1	1.61	12.5	394	86.1
6Ch	2.55	0.15	0.04	0.02	2.42	0.17	0.05	3.1	0.17	1.76	0.05	1.52	3.2	1.58	7.8	716	79.3
7Ch	1.50	0.09	0.08	0.03	2.68	0.22	0.05	3.8	0.22	1.78	0.05	1.38	4.1	1.59	10.1	264	84.6
8NZ	5.30	0.30	0.12	0.04	1.81	0.42	0.14	3.0	0.43	2.16	0.13	1.72	3.3	1.62	8.7	408	23.2
9NZ	6.32	0.45	0.12	0.05	2.58	0.45	0.13	3.4	0.47	1.97	0.13	1.59	3.5	1.68	9.3	420	22.6
10NZ	5.40	0.38	0.11	0.04	2.59	0.46	0.13	3.4	0.47	1.93	0.13	1.75	3.6	1.71	10.1	495	22.1
11Sc	12.77	0.60	0.06	0.03	2.79	0.62	0.10	6.0	0.63	2.64	0.10	2.17	6.1	1.78	17.2	1046	13.5
12Tu	1.79	0.14	0.10	0.03	1.38	0.26	0.08	3.3	0.27	1.86	0.08	1.70	3.4	1.59	8.6	266	40.4
13Tu	1.06	0.20	0.04	0.02	0.89	0.18	0.07	2.5	0.18	1.99	0.07	1.85	2.6	1.47	5.7	199	42.2
14US	2.60	0.09	0.08	0.03	0.76	0.27	0.08	3.1	0.26	1.58	0.08	1.52	3.1	1.52	6.2	363	45.3
15US	1.20	0.18	0.05	0.03	1.82	0.23	0.07	3.2	0.22	1.70	0.07	1.45	3.2	1.50	6.5	259	58.8
16US	3.04	0.37	0.06	0.03	1.28	0.46	0.11	4.5	0.44	2.18	0.10	1.89	4.3	1.67	10.8	510	25.4
17US	4.45	0.49	0.06	0.04	1.24	0.44	0.09	4.1	0.42	2.19	0.10	1.88	4.0	1.61	9.4	378	21.0
18US	3.52	0.31	0.36	0.06	0.96	0.96	0.17	6.1	0.95	1.65	0.16	1.37	6.0	1.47	11.5	181	24.0
19US	2.47	0.26	0.12	0.06	1.10	0.43	0.13	3.3	0.43	1.86	0.13	1.52	3.4	1.56	8.0	507	27.5
20US	2.33	0.28	0.06	0.03	1.49	0.32	0.11	2.9	0.31	2.09	0.10	1.70	3.0	1.60	7.3	310	29.7
21US	7.96	0.41	0.11	0.03	1.44	0.84	0.15	5.7	0.81	1.83	0.15	1.53	5.3	1.77	14.3	757	23.2

L = length, D = diameter, Skew = skewness, AR = aspect ratio, SA = surface area, σ = standard deviation

Table 4. Mineralogy by full pattern fitting XRD analysis along with XRD measurements including ‘cylindrical/prismatic ('CP') index and IR 'OH stretching band ratio', see text for details. XRD and IR data are also given for two reference kaolinites for comparative purposes.

Sample	Quartz	Alunite	Gibbsite	Cristobalite	Kaolinite	Halloysite	d-001	FWHM-001	'CP' index	d-06,33	021,T12	IR OH ratio
1Au	0.3					99.7	7.394	1.10	0.252	1.4857	yes	0.91
2Ch						100.0	7.566	1.30	0.366	1.4835	no	0.38
3Ch						100.0	7.481	1.06	0.260	1.4868	yes	0.81
4Ch	0.1		trace		1.4	98.5	7.667	1.50	0.354	1.4834	no	0.26
5Ch	0.1		0.1			99.8	7.478	1.24	0.326	1.4838	no	0.41
6Ch						100.0	7.593	1.32	0.359	1.4844	no	0.28
7Ch			1.1			98.9	7.403	1.21	0.332	1.4838	no	0.39
8NZ	0.6			0.6		98.8	7.424	1.00	0.267	1.4866	no	1.02
9NZ	7.2			6.8		86.0	7.395	0.97	0.235	1.4875	no	1.17
10NZ	5.8			4.6	1.4	88.2	7.371	0.99	0.249	1.4871	no	1.30
11Sc	0.6					99.4	7.193	0.50	0.083	1.4880	yes	1.41
12Tu	4.0	1.9	2.9		3.2	88.0	7.610	1.48	0.339	1.4852	no	0.57
13Tu	0.8					99.2	7.420	0.88	0.311	1.4855	no	0.54
14US						100.0	7.350	0.90	0.350	1.4839	no	0.50
15US	trace?					100.0	7.478	1.22	0.347	1.4853	no	0.35
16US	1.9				7.7	90.4	7.425	1.17	0.186	1.4871	no	1.14
17US	0.4	0.1			0.5	99.0	7.555	1.41	0.213	1.4873	yes	1.06
18US	0.5				19.4	80.1	7.197	0.65	0.137	1.4879	yes	1.19
19US	0.6	trace			0.6	98.8	7.350	1.12	0.223	1.4863	no	1.08
20US	1.4		4.3		4.8	89.5	7.478	1.34	0.338	1.4864	no	0.55
21US	0.4				6.1	93.5	7.325	0.70	0.172	1.4877	no	1.20
KGa2							7.184	0.33	0.053	1.4891	NA	1.07
KGa1b							7.169	0.25	0.011	1.4882	NA	1.13

Samples 11Sc, 12Tu, and 17US contain traces of phosphate minerals, possibly woodhouseite in 12Tu and 17US
Sample 21 US contains traces of micas

Table 5. Specific surface area (SA), specific pore volume (Vp), and cation exchange capacity (CEC) data.
Pore volume with the range of lumen diameter (5-30nm) is also given, along with the
extent of hysteresis between adsorption and desorption isotherms, and CEC normalized to a surface area of 50 m^2g^{-1}.

Sample	SA_{BET} (m^2g^{-1})	Vp(cm^3g^{-1})	$MFPD_A$ (nm)	Hyd. (nm)	Vp(cm^3g^{-1}) (5-30 nm)	Lumen space (%)	Hyster.(cm^3g^{-1} x Ps/Po)	CEC (cmol(+)kg^{-1})	CEC@50m^2g^{-1}
1Au	62.6	0.29	14.4	18.7	0.124	32.3	1.65	8.0	6.4
2Ch	66.8	0.20	8.9	12.2	0.113	29.4	5.76	6.3	4.7
3Ch	33.7	0.14	16.6	16.5	0.060	15.5	0.46	4.3	6.4
4Ch	80.4	0.24	12.7	12.1	0.151	39.4	9.37	7.6	4.7
5Ch	68.5	0.22	12.7	13.1	0.126	32.7	4.61	7.2	5.3
6Ch	90.6	0.30	15.4	13.4	0.216	56.2	7.56	6.7	3.7
7Ch	69.5	0.27	12.0	15.7	0.121	31.5	7.96	6.1	4.4
8NZ	35.4	0.16	N/A	18.4	0.061	15.8	1.02	3.4	4.8
9NZ	22.5	0.08	N/A	14.6	0.037	9.7	0.14	2.1	4.6
10NZ	27.8	0.12	N/A	17.3	0.044	11.5	0.84	2.0	3.6
11Sc	15.5	0.06	N/A	15.7	0.026	6.7	-0.07	1.6	
12Tu	60.7	0.13	11.3	8.5	0.080	20.7	4.70	6.2	5.1
13Tu	55.6	0.15	13.5	11.0	0.081	21.2	1.54	7.7	7.0
14US	68.4	0.25	14.4	14.8	0.156	40.6	5.68	6.7	4.9
15US	75.7	0.22	14.4	11.8	0.135	35.2	6.45	8.8	5.8
16US	34.0	0.13	14.4	15.5	0.053	13.7	-0.06	3.5	5.2
17US	30.0	0.14	15.4	19.3	0.050	13.1	-0.01	3.5	5.8
18US	35.9	0.24	N/A	26.6	0.057	14.8	1.06	3.8	5.3
19US	36.1	0.18	16.6	20.5	0.074	19.2	1.52	2.9	4.0
20US	74.0	0.13	10.2	7.0	0.081	21.1	3.72	9.3	6.3
21US	28.0	0.10	N/A	13.7	0.043	11.2	-0.20	4.2	7.4

Note CEC for sample 11Sc is calculated not measured.

Table 6. Pearson correlation matrix for the main physical and mineralogical properties measured. Correlation coefficients below diagonal, corresponding P-values above diagonal.

	Fe_2O_3	*Mean L*	*Mean D*	*Mean AR*	*AR10%*	*SA_{calc}*	*SA_{BET}*	Vp	Hyster	CEC	*d-001*	*FWHM-001*	*d-06,33*	*CPindex*	*IR OH ratio*
Fe_2O_3		0.263	0.719	0.130	0.017	0.149	0.048	0.026	0.062	0.097	0.141	0.142	0.091	0.006	0.030
Mean L	0.256		0.000	0.004	0.004	0.004	0.000	0.108	0.001	0.003	0.000	0.000	0.000	0.000	0.000
Mean D	0.084	0.813		0.749	0.535	0.000	0.000	0.013	0.001	0.001	0.005	0.010	0.000	0.000	0.000
Mean AR	0.341	0.601	0.074		0.000	0.666	0.167	0.769	0.105	0.409	0.043	0.062	0.187	0.007	0.064
AR10%	0.514	0.599	0.144	0.907		0.802	0.036	0.380	0.060	0.095	0.060	0.047	0.085	0.001	0.017
SA_{calc}	-0.326	-0.596	-0.842	0.100	-0.058		0.000	0.000	0.000	0.001	0.029	0.030	0.000	0.001	0.000
SA_{BET}	-0.436	-0.726	-0.747	-0.313	-0.459	0.773		0.000	0.000	0.000	0.004	0.003	0.000	0.000	0.000
Vp	-0.485	-0.361	-0.532	0.068	-0.202	0.752	0.745		0.001	0.006	0.297	0.155	0.001	0.017	0.002
Hyster	-0.414	-0.684	-0.681	-0.363	-0.417	0.725	0.897	0.685		0.001	0.007	0.006	0.000	0.000	0.000
CEC	-0.372	-0.611	-0.672	-0.190	-0.374	0.651	0.894	0.576	0.678		0.023	0.022	0.001	0.000	0.000
d-001	-0.332	-0.716	-0.585	-0.445	-0.417	0.477	0.601	0.239	0.571	0.493		0.000	0.005	0.000	0.001
FWHM-001	-0.332	-0.703	-0.548	-0.414	-0.437	0.475	0.615	0.322	0.580	0.496	0.913		0.006	0.000	0.002
d-06,33	0.378	0.787	0.811	0.300	0.385	-0.851	-0.857	-0.686	-0.893	-0.682	-0.592	-0.578		0.000	0.000
CPindex	-0.582	-0.868	-0.697	-0.574	-0.653	0.679	0.862	0.516	0.808	0.756	0.737	0.706	-0.858		0.000
IR OH ratio	0.473	0.810	0.804	0.411	0.515	-0.771	-0.939	-0.625	-0.894	-0.845	-0.685	-0.639	0.903	-0.918	

L = length, D = diameter, AR = aspect ratio, SA = surface area, Vp = pore volume, Hyster = hysterisis